Learning transcriptome dynamics for discovery of optimal genetic reporters of novel compounds

Aqib Hasnain*[1], Shara Balakrishnan[2], Dennis M. Joshy[1], Steven B. Haase[3], Jen Smith[4], and Enoch Yeung[1]

[1]Department of Mechanical Engineering, University of California Santa Barbara
[2]Department of Electrical and Computer Engineering, University of California Santa Barbara
[4]California Nanosystems Institute, University of California Santa Barbara
[3]Department of Biology, Duke University

Abstract

Accelerating the design of synthetic biological circuits requires expanding the currently available genetic toolkit. Although whole-cell biosensors have been successfully engineered and deployed, particularly in applications such as environmental and medical diagnostics, novel sensing applications necessitate the discovery and optimization of novel biosensors. Here, we address this issue of the limited repertoire of biosensors by developing a data-driven, transcriptome-wide approach to discover perturbation-inducible genes from time-series RNA sequencing data, guiding the design of synthetic transcriptional reporters. By combining techniques from dynamical systems and control theory, we show that high-dimensional transcriptome dynamics can be efficiently represented and used to rank genes based on their ability to report the perturbation-specific cell state. We extract, construct, and validate 15 functional biosensors for the organophosphate malathion in the underutilized host organism *Pseudomonas fluorescens* SBW25, provide a computational approach to aggregate individual biosensor responses to facilitate enhanced reporting, and exemplify their ability to be useful outside the lab by detecting malathion in the environment. The library of living malathion sensors can be optimized for use in environmental diagnostics while the developed machine learning tool can be applied to discover perturbation-inducible gene expression systems in the compendium of host organisms.

Introduction

The aim of synthetic biology is to design and construct living systems to possess desired functionality; this is done by developing, characterizing, and assembling biological parts in cells, creating living devices [1]. Synthetic biological circuits were first engineered in the year 2000 when Gardner et al. [2] constructed a two-node genetic bistable switch and Elowitz and Leibler [3] constructed a three-node genetic oscillator (known as the repressilator), paving the way for fine-tuned control of gene expression. Since, notable breakthroughs have emerged in post-transcriptional and translational control [4–6], optogenetic control [7], eventually leading to control of metabolic pathways [8,9] and neural-like computing [10]. Although the aforementioned genetic circuits exhibit distinct behavior, their design is implemented with a shared set of biomolecular parts, limiting the range of functionality that can be achieved.

As was the case for the genetic switch and repressilator, much of the engineering workflow for optimizing the design of genetic circuits has relied on iteratively replacing parts to minimize discrepancies between actual and desired behavior [11–13]. By parts, we are referring to DNA sequences which comprise the elementary building blocks of genetic circuits; for example, protein-coding genes, promoters, terminators, and ribosome binding sites to name only a few [12]. The initial pool of parts that were curated for use by synthetic biologists in bottom-up design were largely derived from *E. coli* and since has expanded into a library containing parts from a diverse set of microorganisms, from bacteriophage [14] to yeast [15].

The expansion of the genetic toolkit for circuit design remains an ongoing challenge as substantial effort is required to mine, design, characterize, and optimize biological parts [16–20]. While a significant amount of attention has been placed on optimizing and characterizing existing biological parts for genetic circuit design, less attention has been placed on mining biological parts. This has resulted in much needed insulation and biological orthogonalization strategies [21] for mitigating inadvertent intra-circuit and inter-circuit-host interactions. Moreover, programmatic tools have been developed to automate the design of genetic circuits that implement logical operations using a set of well-characterized parts in model organisms [22–25]. However, since biological parts and circuits are characterized and optimized within a single model organism and often not evaluated in application relevant organisms, there is no guarantee that the parts can be "taken off the shelf" for use in engineering novel host organisms. An increased focus on mining biological parts from novel host organisms will provide an expansion of the existing genetic toolkit from which synthetic biologists can browse and select from.

Transcriptional genetic sensors are a class of biological components that control the activity of promoters [26] and have been used to construct whole-cell (living) biosensors [27–29]. A large portion of transcriptional sensors rely on transcription factor-promoter pairs [30] and have been used in whole-cell biosensing for detection of heavy metals [31], pesticides and herbicides [32–34], waterborne pathogens [35], disease biomarkers [36, 37], and many more applications discussed in [38]. Since microbes are found in virtually all terrestrial environments, one could imagine

*Please address correspondence to aqib@ucsb.edu

that there would be no shortage of transcriptional genetic sensors for novel sensing applications. However, given a novel sensing application for a target compound or perturbation, transcriptional genetic sensors are typically unknown *a priori*. Moreover, a complete methodology for discovering sensors for the target analyte in novel organisms does not yet exist.

The transcriptional activity of an organism can be measured through RNA sequencing (RNA-seq) to produce a snapshot of the bulk cell state subject to intrinsic and extrinsic perturbations. The typical approach for identifying upregulated and downregulated genes across experimental conditions is to apply differential expression analysis [39, 40]. A major pitfall with differential expression analysis is its lack of statistical power when faced with a sparse number of biological replicates. That is to say that the false-positive rate increases drastically when only a small number of biological replicates are available [41] as is often the case due to the costliness of RNA-seq. A related issue arises in that one must sacrifice time points for biological replicates, reducing the fidelity of the dynamical process being studied. As most biological processes are dynamic, time-series profiles are essential for accurate modeling of these processes. Furthermore, differential expression analysis provides no information beyond which genes are upregulated/downregulated [42]. An analysis of expression dynamics provides a potential route to design a sensing scheme for a target analyte for which no single sensor exists.

A typical RNA-seq dataset contains hundreds to tens of thousands of genes; despite that, a subset of genes, which we call *encoder genes*, are typically sufficient for representing the underlying biological variation in the dataset. This is explained by the fact that variations in many genes are not due to the biological process of interest [43] and that many genes have correlated expression levels [44]. The task of identifying a subset of the state (genes) which recapitulate the entire state (transcriptome/cell state) and explain the variations of interest is well studied in the field of dynamics and controls in the form of optimal filtering and sensor placement [45, 46]. In the context of dynamic transcriptional networks, sensor placement is concerned with inferring the underlying cell state based on minimal measurements; this introduces the concept of observability of a dynamical system [47]. The transcriptome is observable if it can be reconstructed from the subset of genes that have been measured. In other words, these genes *encode* the required information to predict the dynamics of the entire transcriptome. Hence the name, *encoder genes*. To the best of our knowledge, measures of observability have not been applied to genetic networks to identify genetic sensors, biomarkers, or other key genes.

Overall, a systematic approach for identifying genetic sensors from RNA-seq datasets is still an open and challenging issue. In this work, we develop a machine learning methodology to extract numerous endogenous biological sensors for analytes of interest from time-series gene expression data (Figure 1). Our approach consists of three key steps, each of which is depicted in the middle panel of Figure 1. Briefly, the first step adapts dynamic mode decomposition (DMD) [48–50] to learn the transcriptome dynamics from time-series RNA-seq data. Beyond the scope of sensor discovery, we show how the dynamic modes can be utilized to cluster genes by their temporal response. The second step involves assigning sampling weights to each gene that quantify the contribution to maximizing observability of the cell state [47, 51, 52]. The sampling weights provide a machine learned ranking of the genes based on their contribution to observability of the system, and using this ranking, encoder genes may be selected. To ensure the ranking is identifying genes which can recapitulate the cell state, the final step is to measure how well a chosen subset of genes can reconstruct the cell state. To validate our proposed methodology, we use our method to generate a library of 15 synthetic genetic reporters for the pesticide malathion [53–55], an organophosphate commonly used for insect control, in the bacterium *Pseudomonas fluorescens* SBW25. The library is composed of encoder genes identified by our proposed machine learning methodology. The transcriptional sensors play distinct biological roles in their host and exhibit unique malathion response curves. Our method uses no prior knowledge of genes involved in malathion sensing or metabolism. Moreover, we use no data source beyond RNA-seq, thereby providing a cost and computationally efficient approach for transcriptional sensor identification.

Results

Induction of malathion elicits fast host response. To start, we will first introduce the time-series RNA-seq dataset that we will use throughout this work. The transcriptional activation and repression of the soil microbe *Pseudomonas fluorescens* SBW25 was induced by malathion at a molar concentration of 1.29 μM (425 ng/μL) for the following two reasons: i) it is a moderate amount that can typically be found in streams and ground water after recent pesticide use based on studies done in the United States, Malaysia, China, Japan, and India [56, 57], and ii) the characteristic concentration of a metabolite in bacteria is on the order of $0.1-10$ μM [58]. Malathion is an organophosphorus synthetic insecticide used mainly in agricultural settings [59] while SBW25 is a strain of bacteria that colonizes soil, water, and plant surface environments [60]. This makes the soil-dwelling strain a prime candidate for identification of transcriptional genetic sensors for the detection of malathion.

To enable rapid harvesting and instantaneous freezing of cell cultures, we made use of a custom-built vacuum manifold, enabling fast arrest of transcriptional dynamics (Supplementary Figure 6 and Methods). Following malathion induction, cells were harvested at 10 minute intervals for 80 minutes, obtaining a total of 9 time points across two biological replicates that were sequenced. As the focus of our study is on identifying trends and correlations across time, we heavily favored time points in the trade-off between time points and biological replicates. To identify candidate sensor genes for malathion induction and subsequently build synthetic transcriptional reporters, we also collected samples from a cell culture that was not induced with malathion. See the Methods section for further details on cell culturing and harvesting.

RNA sequencing (RNA-seq) provides a snapshot of the entire transcriptome i.e. the presence and quantity of RNA in a sample at a given moment in time. In this work, we examine the fold change response given by first normalizing the raw counts to obtain transcripts per million (TPM) [61] followed by calculating the fold change of the malathion condition with respect to the negative control. The implication is that the fold change is the cell state, $\mathbf{z}_k$ for some time point k, we are concerned with for discovery of genetic sensors. Of the nearly 6000 known genes in the SBW25 genome, a large fraction of them were not expressed at significant levels. Specifically, only 10% of or 624 genes are kept for modeling and analysis due to their relatively high abundance.

Given our goal of extracting salient biosensors from time-series gene expression data, we first model the dynamical process that is driven by the input of malathion on the SBW25 transcriptome. We consider malathion as a step input to the cell culture and as an impulse to the cells. This is motivated by the fact that biomolecular systems often respond to the *derivative* of the input and not the input itself (e.g. the absolute concentration

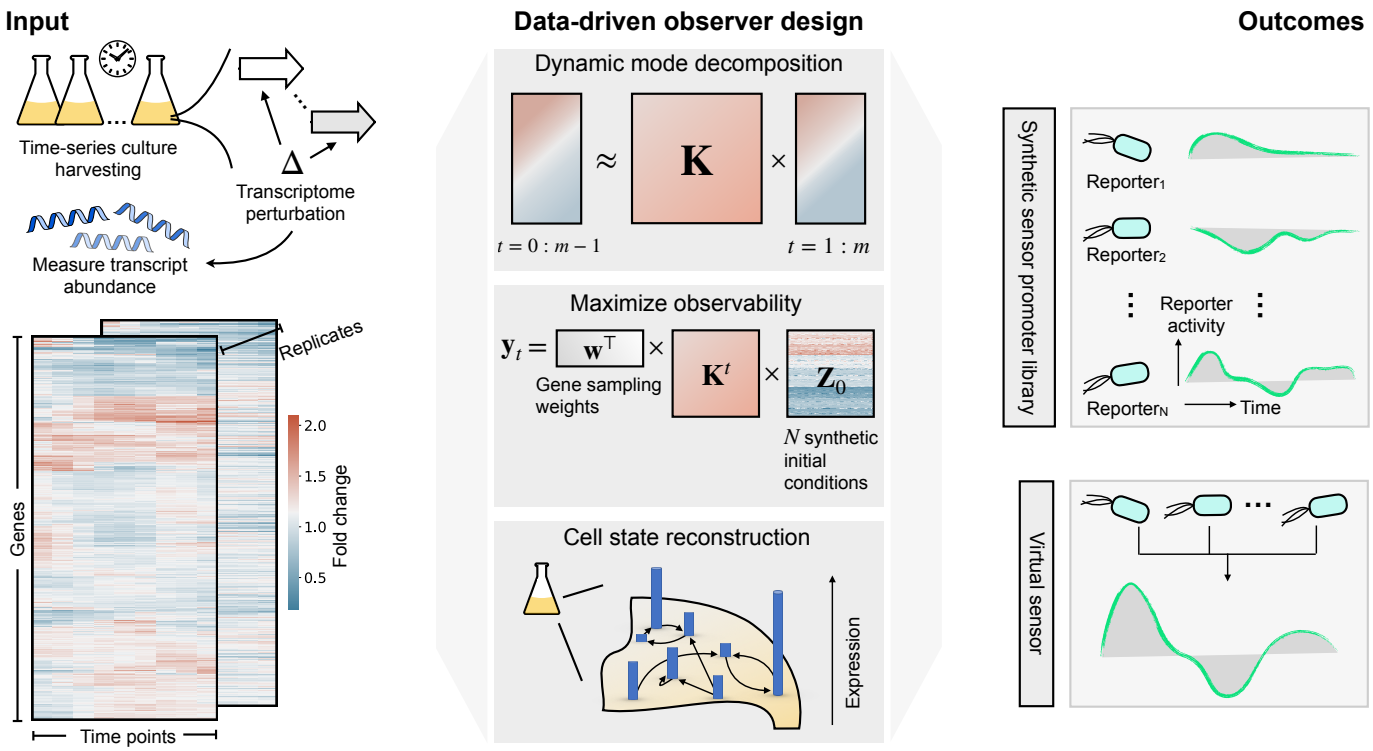

Figure 1: **Transcriptional genetic sensors underlying the response from environmental perturbations can be extracted using data-driven sensor placement.** Bulk RNA sequencing (RNA-seq) measures transcript abundance over time following transcriptome perturbations. Our method starts by applying dynamic mode decomposition (DMD) to the fold change response to discover dynamic modes which govern the evolution of the cell state. The dynamic modes are used to design a state observer (gene sampling weights) that maximize the observability of the transcriptome dynamics. Measurements from a subset of genes (*encoder genes*) informed by the gene sampling weights are then used to reconstruct the cell state. Our method returns: 1) a dynamics matrix (or equivalently, a set of dynamic modes) describing how expression of gene i at time t is impacted by gene j and time $t-1$. and 2) gene sampling weights. The outcome, demonstrated in this work, is a library of synthetic sensor promoters (genetic reporters) that are used to detect an analyte of interest. Since each genetic reporter has a unique response to the same perturbation, the library can be artificially fused to produce a purely virtual sensor for enhanced reporting.

of malathion) [62, 63]. In the next section, we apply dynamic mode decomposition (DMD) to approximate the fold change response with a sparse collection of dynamic modes. Specifically, we demonstrate how DMD can accurately describe gene expression dynamics by decomposing the time-series gene expression into temporally relevant patterns.

Dynamic mode decomposition uncovers modes of host cell response.

Dynamic mode decomposition (DMD) is a time-series dimensionality reduction algorithm that was developed in the fluid dynamics community to extract coherent structures and reconstruct dynamical systems from high-dimensional data [48]. Recently, several works have adapted and applied DMD to biological systems in various contexts [64–68], choosing DMD for its ability to i) reproduce dynamic data over traditionally static methods such as principal component [69] or independent component analysis [70] and ii) represent the dynamics of high-dimensional processes (e.g. gene interaction networks) using only a relatively small number of modes.

To uncover the diverse modes of the host cell response to malathion induction, we performed (exact) DMD [50] on the transcriptomic dataset (see Methods for the details). Specifically, we perform DMD on the standardized fold change, defined as $\bar{z}_g = \overline{x_g^{\text{malathion}}/x_g^{\text{control}}}$, where x_g is the expression (in TPM) of gene g and the overbar represents a variable which is transformed to have zero mean and unit variance. DMD allows the learning of low-dimensional linear models from high-dimensional time-series data. Briefly, this implies that quantitative features of a nonlinear model are not captured in our model, e.g. multiple equilibria, and chaos. If these nonlinear features are relevant to the system being studied, one can extend DMD to capture arbitrary nonlinearities, at the cost of needing a larger number of samples [71]. In this section we will describe how modeling the fold change response with DMD enables the identification of biologically relevant temporal patterns that are driven by the malathion perturbation. In the following sections we will show that the modes of the fold-change response will allow us to identify genes which act as reporters for the malathion specific response.

DMD captures transcriptome dynamics by decomposing a gene expression matrix (genes × time points) into dynamic modes — each mode characterizes damped, forced, and unforced sinusoidal behavior. Namely, each dynamic mode is associated with a growth or decay rate and a fixed frequency of oscillation. The reconstruction of the impulse response of the fold change dynamics is schematically represented in Figure 2a. The heatmap $\mathbf{V}$ represents the matrix of 10 learned dynamic modes, each of which has rate of growth or decay and oscillation frequency given by a single corresponding DMD eigenvalue in $\mathbf{\Lambda}$, and mode amplitude given in $\mathbf{b}$. As they are complex-valued, the magnitude and

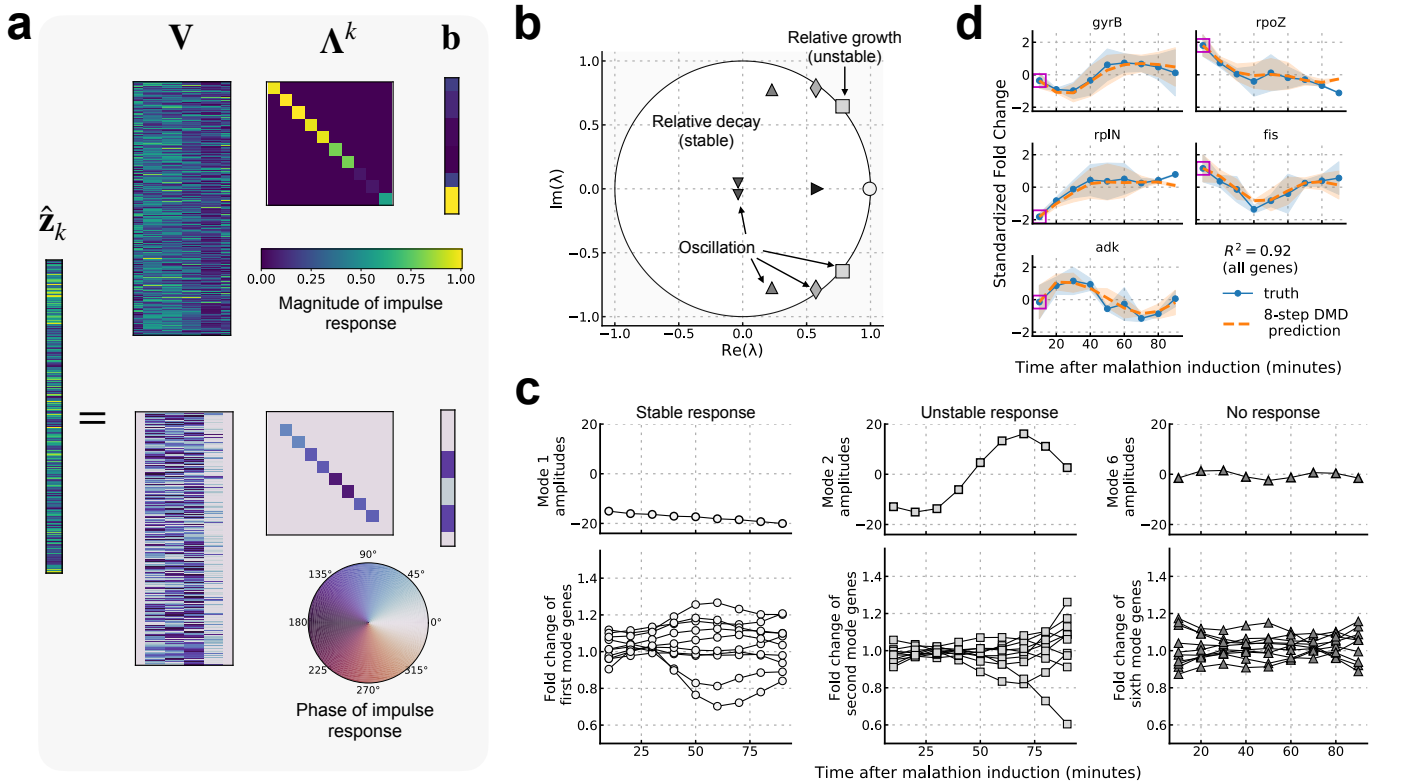

Figure 2: **Dynamic mode decomposition provides an interpretable and predictive model of gene expression dynamics.** **(a)** DMD reconstruction of the fold change dynamics subject to an impulse input of malathion. Since the modes are complex-valued, their magnitude and phase are separately visualized. The vector $\hat{\mathbf{z}}_k$ is the reconstruction of the fold change at time k, given by the depicted spectral decomposition where $\mathbf{V}$ are the DMD modes, $\mathbf{\Lambda}$ are the DMD eigenvalues, and $\mathbf{b}$ are the mode amplitudes (see Methods for detailed description of DMD). **(b)** The DMD spectrum reveals the growth, decay, and oscillation of each of the 10 dynamic modes that comprise the transcriptomic dataset. Each marker is an eigenvalue, and its diameter is proportional to the magnitude of the corresponding dynamic mode. Eigenvalues inside the unit circle correspond to decaying dynamics, eigenvalues with nonzero imaginary part correspond to oscillatory dynamics, and eigenvalues outside the unit circle correspond to growing dynamics. **(c)** The eigenvalue scaled amplitudes, $\lambda_i^k \mathbf{b}_i$, of modes 1, 2, and 6 are visualized (upper) along with the 10 genes whose dynamics are most impacted by each of the modes (lower). The marker used for each mode indicates which eigenvalue it corresponds with in **(b)**. **(d)** The eight-step prediction is visualized for five randomly selected genes in the transcriptomic dataset. The error bars represent the sample standard deviation across two biological replicates (blue solid curve) and across predictions (orange dashed curve). Magenta squares overlapping each gene's initial condition are indicating the data that is provided to make predictions. The coefficient of determination, R^2, for the eight-step prediction across all genes is computed to be 0.92.

phase of each DMD mode, eigenvalue, and amplitude is visualized separately. The magnitude of each DMD mode represents gene-wise coherent activation while the phase represents the relative shift of this activation for the damped (or forced) modes. Here 10 modes are chosen as it is a minimal set of modes that can accurately capture the dynamics while also limiting the presence of instabilities in the model (Supplementary Figure 1). With fewer modes the instabilities disappear, however the model accuracy decreases. With more modes, the accuracy asymptotically approaches 100%, however the number of instabilities increases.

Our DMD analysis of RNA-seq data uncovers three distinct modal responses, namely stable, oscillatory, and unstable, and the response of each modes is characterized by the corresponding DMD eigenvalue, $\lambda = a + bi$ (here $i = \sqrt{-1}$). The real part, a, and the imaginary part, b, are what determine the growth (unstable)/decay (stable) rate and the frequency of oscillation, respectively. We have plotted the 10 DMD eigenvalues relative to the unit circle in Figure 2b and labeled the eigenvalues according to their type. Note that in our model a single eigenvalue is either both stable and oscillatory, unstable and oscillatory, or only stable. Also, since our data are real-valued, any complex eigenvalue must be associated with a complex conjugate pair, explaining the symmetry across the real axis in Figure 2b.

The first type of mode that we recover is stable and are characterized by eigenvalues which are inside the unit circle. The magnitude of eigenvalues inside the unit circle are strictly less than one and such a set of stable modes indicate relative decay, that is to say that many genes have a temporal response which only transiently deviate from a neutral fold change (fold change equal to one for non-standardized trajectories and fold change equal to zero for standardized trajectories). Stable modes that have eigenvalues nearer to the unit circle are capturing majorly uninhibited genes, while stable modes that are nearer to the origin are capturing genes which converge to neutral fold change exponentially, i.e. they exhibit strong relative decay in their fold change.

The second type of dynamic mode we uncover is oscillatory and are characterized by by eigenvalues with nonzero imaginary part. Since gene expression data is always real-valued, oscillatory modes will always come in complex conjugate pairs. Each pair of complex-valued modes then describes a fixed frequency of oscillation, and each gene's dynamics can be reconstructed from one

or more of these frequencies. The work of Sirovich found that the oscillatory modes obtained from DMD represent the genes underlying the yeast cell cycle, and the frequencies of oscillation were shown to provide an estimate of the cell cycle period that agrees with the literature [66].

The third and final type of mode we recover is an unstable response characterized by eigenvalues whose magnitude is larger than one. Driven by the impulse input of malathion, many genes show temporal response that were either upregulated or downregulated. If the upregulation and downregulation is persistent throughout the gene's temporal profile or occurs at later times, there must be at least a single mode with eigenvalue outside the unit circle to be able to capture the underlying unstable response. This is because DMD is essentially learning a linear state-space representation of the fold change response and a linear system can only exhibit three types of limiting behaviors, i) convergence to the origin (stable), ii) periodic orbits, and iii) divergence to infinity (unstable). Therefore, for the reconstruction accuracy to be maximized, DMD eigenvalues with magnitude larger than one may be necessary. Such eigenvalues are marked with relative growth in Figure 2b. Though the eigenvalues are outside the unit circle, they are only marginally so, implying that unstable trajectories make up only a small portion of the transcriptomic response to malathion.

Despite the fact that most genes require a superposition of all of the dynamic modes for accurate reconstruction, we show that the modes can successfully group genes into interpretable clusters. Figure 2c (upper) shows the evolution of three dynamic modes representative of the transcriptomic dataset: modes 1, 2, and 6, corresponding to stable (modes 1 and 6) and unstable (mode 2) directions in gene space. The genes which are most influenced by each of these modes are obtained from the columns of the DMD modes $\mathbf{V}$ and are plotted in the lower part of Figure 2c.

The genes which are most influenced by mode 1 are those which diverge, in a stable manner, from a neutral fold change while the genes most influenced by mode 2 are those which diverge away from neutral fold change, capturing unstable trajectories. This is consistent with the eigenvalues of mode 1 and mode 6, which are stable and unstable, respectively. Finally, the genes most influenced by mode 6 are those with no clear trend present in their dynamics. In the next section, we will characterize those genes which contribute to cell state reconstruction and act as reporters for the malathion specific response. Relatedly, of the 20 genes that are most impacted by mode 1, seven of these genes contribute highly to cell state reconstruction (they are within the top 20 genes that contribute to the observability of the system).

The model of the gene expression response to malathion that we have learned using DMD has been shown to be interpretable, clustering genes with distinct temporal responses. To instill confidence in the model, we measure the accuracy of reconstruction using the coefficient of determination, R^2, as the metric. The R^2 is computed by feeding an initial condition (the gene expression at time $t = 0$) to the model and then predicting all subsequent time points; for the nine time points in the dataset, this amounts to two eight-step predictions across the biological replicates. Specifically, the reconstruction is computed precisely as depicted in Fig 2a where $\mathbf{V}$, $\mathbf{\Lambda}$, and $\mathbf{b}$ are held constant and only the time k is updated to obtain the DMD estimate of the bulk cell state at time k. We emphasize that this is distinct from measuring model accuracy by computing a one-step prediction for each time point, which gives very little information about the dynamic process that has been captured. We obtain an R^2 of 0.92, showcasing that the low-dimensional model learned via DMD has accurately captured the dynamics of the fold change response. To provide a foundation for understanding when linear models can accurately represent fold change dynamics, we have shown, in the Supplementary Information, that the fold change response of two linear systems, under stated assumptions, can be represented as the solution of a linear system.

The results of this section demonstrate that the set of 10 recovered DMD modes, eigenvalues, and amplitudes are indeed biologically relevant to the dynamics of the malathion response in the window of time that we have sampled the transcriptome. The DMD model predictions for five randomly selected genes in the SBW25 transcriptome are depicted in Figure 2d. These five genes each exhibit a distinct response, and each are well captured by our DMD model. Though only five genes are presented, the result is representative of the whole transcriptome prediction. A key point then is that gene expression dynamics sampled at the resolution of minutes can be well approximated by a linear dynamical system, i.e. by a set of exponentially shrinking and growing modes. In what follows, we develop a sensor placement framework, relying on the learned linear dynamical system, to generate a ranked list of encoder genes, i.e. subsets of genes which show variation to malathion induction and that can recapitulate the cell state.

Sensor placement for cell state inference and extraction of genetic sensors. Gene interaction networks are complex systems that induce systematic interdependencies between genes. That is to say that the expression of most genes, if not all, depends on the expression of at least one more genes in the network. These interdependencies make it possible to measure only a subset of genes to infer the behavior of all other genes [72]. In this section, we will show that time-series measurements of a subset of genes, called *encoder genes*, are sufficient to capture the entire cell state, making the system observable. The system we are referring to is the transcriptome or fold change dynamics that we now have a DMD representation for and it is observable when the complete initial cell state, $\bar{\mathbf{z}}_0$, can be uniquely inferred from output measurements $\mathbf{y}_k$, for times $k = 1, 2, ..., T$, where the measurements are linear combinations of the expression of all genes (see Methods).

The approach taken in this work for evaluating whether a gene is an encoder of complete cell state information is to quantify how much each gene contributes to observability. To do this, we optimize a scalar measure of the observability gramian, a matrix which determines the amount of information that a set of sensors can encode about a system. In the context of transcriptome dynamics, given the DMD representation of the dynamics and a chosen gene sensor placement, the gramian quantitatively describes i) to what degree cell states are observable and ii) which cell states cannot be observed at all. Increasing i) while decreasing ii) is the aim of many sensor placement techniques; furthermore, many scalar measures of the gramian have been proposed to determine the sensor placement which maximizes the observability of the underlying dynamical system [73–75].

To provide a method which is capable of handling high-dimensional networks, we optimize the *signal energy*, $\sum_{i=0}^{T} \mathbf{y}_i^\top \mathbf{y}_i$, of the underlying system as it does not require explicit computation of the observability gramian. Computing gramians from unstable and/or high-dimensional systems is computationally expensive and hence we choose to use the measure which can scale for a wide array of biological datasets collected from diverse host organisms. To further emphasize this point, we note that we are implicitly optimizing over 5.5×10^{29} sensor placement combinations, if we choose to select 15 genes from the full set of 624 (624 choose 15). The strategy we employ is to assign gene sampling

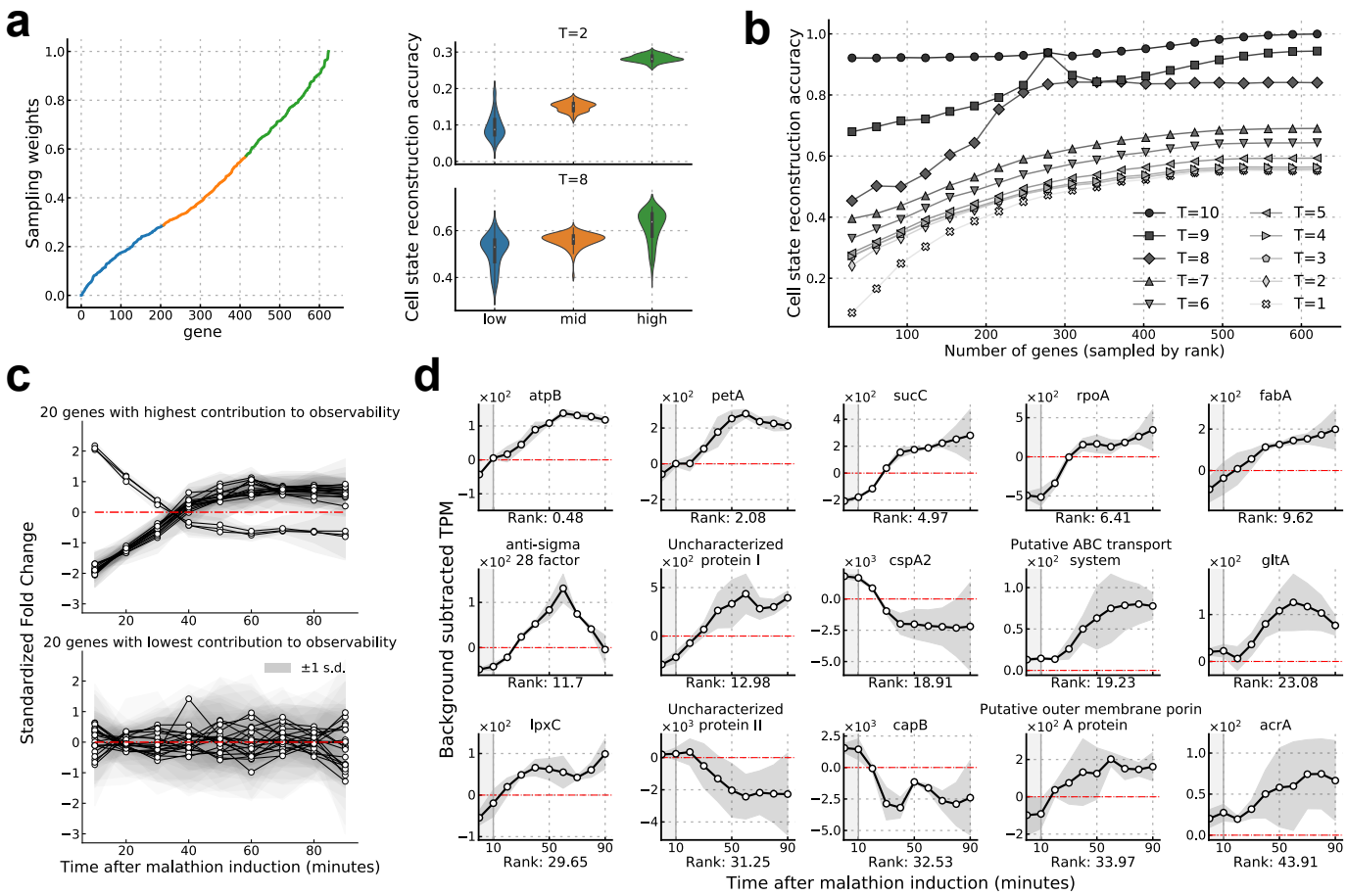

Figure 3: **Gene sampling weights which maximize observability provide a machine learned ranking for extraction of genetic sensing elements. (a)** The gene sampling weights $\mathbf{w}$ are sorted by value and plotted in the left panel. The weights are grouped into three categories: i) the third of genes with highest magnitude of sampling weights (plotted in green), ii) the third of genes with second highest magnitude of sampling weights (plotted in orange), and ii) and the lower third that remains (plotted in blue). The right panel depicts the reconstruction accuracy (R^2) between the true initial condition and the estimated initial condition when sampling 50 genes at random from each of the aforementioned groups for (top) $T = 2$ time points and (bottom) $T = 8$ time points. The reconstruction accuracy was measured for a total of 100 runs each with a distinct set of 50 genes from each group. **(b)** Reconstruction accuracy between the estimated initial condition $\hat{\mathbf{z}}_0$ and the actual $\bar{\mathbf{z}}_0$ is plotted for number of sampled time points $T = 1$ to $T = 10$. Each data point is obtained by sampling genes by rank (the amount sampled is given on the x-axis), generating outputs for T time points, and then estimating the initial condition. **(c)** The fold change response of the 20 genes which contribute most (top) and least (bottom) to the observability of the initial cell state are plotted. The error bars represent the sample standard deviation across two biological replicates. **(d)** The background subtracted TPM (malathion (TPM) − negative control (TPM)) of the 15 encoder genes selected from the proposed ranking – by contribution to observability. The label on each x-axis indicates the percentage rank (out of 624 genes) of the gene, with respect to the gene sampling weights, and zero here being the highest rank. The error bars indicate the sample standard deviation across two biological replicates. Malathion was introduced to the cultures after collecting the sample at 0 minutes, hence this sample is not used for modeling and cell state inference and this time window is shaded in gray.

weights, w_g, to each gene g through optimizing sensor placement, i.e. maximizing the signal energy. The significance of the magnitude of each weight is to rank each gene by their contribution to observability, i.e. higher magnitude denotes higher contribution. The Methods section provides quantitative details on the relationship between observability, the observability gramian, and signal energy for sensor placement.

By examining the learned gene sampling weights, we found that nearly all 624 modeled genes contribute, some insignificantly, to the observability of the system. Displayed in Figure3a (left) are the magnitude of gene sampling weights, $\mathbf{w}$, whose elements have been scaled to be in the range 0 to 1, that maximize the observability of the cell state. We note that the relative magnitude of the weights are what is important, therefore any linear scaling will preserve the information that are contained in the weights. Weights that are negative-valued (not shown here) correspond to downregulated genes and weights that are positive-valued correspond to genes that are upregulated. The higher the magnitude of the gene sampling weight, the more important the gene is likely to be for cell state reconstruction. To test this notion, the sampling weights are artificially grouped into three categories, distinguishing genes which correspond to the top (green), middle (orange), and lower (blue) third for magnitude of sampling weights. Each category contains 208 genes, and next we show the gain in information that can be achieved when sampling from one category over another.

To examine the contribution to observability provided by genes in each of the categories, we perform Monte Carlo simulations to estimate the expected predictability of the initial cell state. From output measurements, $\mathbf{y}_i$ $(i = 1, 2, ...T)$, that are generated by randomly sampling 50 genes from a specified category (low, mid, high), the cell state, $\bar{\mathbf{z}}_0$, is estimated and the coefficient of determination (R^2) between the actual and estimated cell state is computed as a measure of reconstruction accuracy. The simulation is repeated 1000 times for each category and the resulting distributions over the random gene sets are plotted in Figure 3a (right). In the top panel, we can see that when $T = 2$ (2 time points are used for reconstruction), predictability of the cell state is low in all cases, and it is highest for the genes in the high category. Specifically, the reconstruction accuracy is three and two times larger in the high category than in the low and mid categories, respectively. Similarly, when the number of time points, T, is increased to eight, exhausting the time points we are modeling before extrapolation, the genes in the high category best reconstruct the cell state. We found that the low and mid category genes are also capable of significant reconstruction of the cell state, exemplifying that there is a rich amount of information encoded in the dynamics. This further highlights the importance of carefully designing experiments that are sufficiently rich in conditions and time points.

Measuring fewer genes for many time points leads to higher cell state reconstruction accuracy than if many genes are measured for fewer time points. This result is demonstrated in Figure 3b which shows how the cell state reconstruction accuracy is affected by two parameters, the number of sampled genes and the number of time points, T, that the genes are measured for. The reconstruction accuracy is again the coefficient of determination, R^2, between the reconstructed initial condition, $\hat{\mathbf{z}}_0$, and the actual initial condition $\bar{\mathbf{z}}_0$. For each T, the first data point is generated by sampling only the five genes with the highest sampling weights for T time points. The complete cell-state is then inferred from these measurements alone and the coefficient of determination between the estimated and actual cell state can be computed (see Methods for a detailed description of the cell state inference algorithm). To compute subsequent data points, the next five genes with maximum sampling weights are simultaneously measured along with previously measured genes, and the cell state is reconstructed again. For the response of SBW25 to malathion, we find that even if only the top five genes are measured but for $T = 10$ time points, the cell state reconstruction is still more accurate than if all genes with nonzero sampling weights are measured with $T \leq 8$ time points. This signifies that the ability to study the dynamics of a few genes with fine temporal resolution can greatly increase the knowledge of the entire system.

Failure to reconstruct the initial cell state is a result of two mechanisms. The first is that we only have access to the DMD representation of the dynamics, not the true dynamics. Therefore, any output measurements generated using the DMD model will certainly incur an error with respect to the actual dynamics. As error accumulates each time-step, it is possible for the reconstruction accuracy to decrease with increasing time points. In addition to this, if a gene is added to the set of sensors, yet its dynamics are poorly predicted by the model, then it can drag down the cell state reconstruction accuracy. This can be observed in two curves in Figure 3b, namely for $T = 10$ and $T = 9$. The second hindrance for full cell state reconstruction is when many genes contain redundant information. If two genes have nearly identical gene expression profiles, adding the second gene to the set of measurements provides no useful information for the cell state inference. This may explain the asymptotic behavior of the curves in Figure 3b. There are only relatively few distinct dynamic profiles present in the transcriptomic dataset, and once all distinct profiles have been sampled, no further improvement in reconstruction can occur. This explanation is consistent with the fact that many genes co-express [44] and this fact has even been used to reconstruct dynamic gene regulatory networks [76].

The gene sampling weights, $\mathbf{w}$, provide a machine learned ranking for discovering genetic sensors. Recall that the fold change was taken to be the state of the system when performing DMD. In so doing, we show that the encoder gene ranking can also predict genes that respond to malathion in a condition specific manner. Specifically, genes which contribute highly to the observability of the system are genes which show prolonged dysregulation in the presence of malathion. This is visualized in Figure 3c where in the top panel the 20 genes which have the largest sampling weights are plotted. Each of the 20 genes show dysregulation from the neutral fold change (0) that is persistent over the course of the time-series. Conversely, the 20 genes with lowest sampling weights show no clear trend or signal of dysregulation.

To show that encoder genes can act as genetic reporters for malathion, we selected a set of 15 genes with which to construct transcriptional reporters from. The 15 time-series profiles generated via RNA-seq (malathion TPM - control TPM) are visualized in Figure 3d. To select this set of 15, the genes were first ranked (out of 624 genes) based on their gene sampling weights with 0 being the highest. Then a randomly chosen subset of 15 genes from the top half of the ranking were used to reconstruct the cell state. The subset of 15 which produced the highest cell state reconstruction accuracy, i.e. which maximize the observability of the cell state, were chosen as the encoder genes with which to design genetic reporters from. Specifically, the observability maximizing set of 15 genes shown in Figure 3d achieve a cell state reconstruction accuracy of 76% when outputs are generated using $T = 8$ time points. Of the 15 selected encoder genes, 12 appear to be activated by induction of malathion while the remaining 3 appear to be repressed.

The selected encoder genes are involved in disparate biological processes. Table 1 lists the molecular functions of each of the selected genes based on their Gene Ontology (GO) annotations [77]. Where gene names are not available, we have used protein annotations to denote those genes. It is shown that the set of molecular functions are diverse, indicating that malathion drives the activation and repression the disparate biological processes. This is precisely the goal of our sensor placement framework, to select genes which not only show variation to the biological process of interest and recapitulate the cell state, but also to select genes which are involved in distinct dynamical processes. When synthesized into genetic reporters, as we will show next, these encoder genes exhibit distinct dynamic range, sensitivity, and time-scales in response to malathion.

Design and characterization of fluorescent malathion sensors.

To validate the transcriptome-wide analysis for identification of biosensors, the putative promoters of the candidate sensor genes were cloned into a reporter plasmid containing a reporter gene encoding *sfGFP* (superfolder green fluorescent protein) and transformed into the host SBW25 (Figure 4a). The reporter strains are cloned in an unpooled format, allowing for malathion response curves to be generated at the reporter level as opposed to a pooled study which would incur additional sequencing costs for individual strain isolation.

Malathion reporters are characterized in the laboratory in an

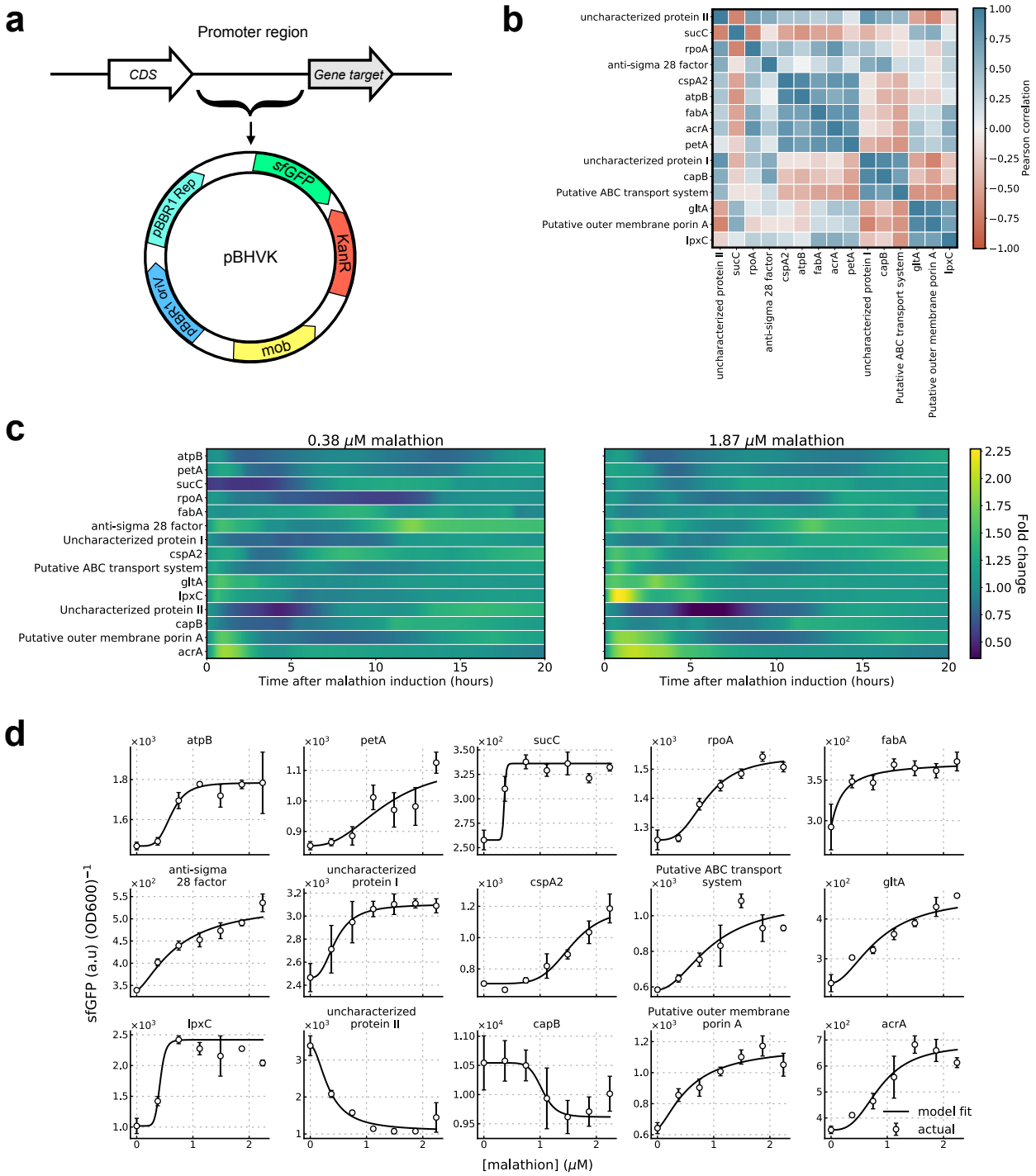

Figure 4: **Our machine learning approach successfully extracted 15 sensors, each with distinct malathion response curves.** **(a)** A map of the plasmid, pBHVK, used to construct the library. The plasmid contains a kanamycin resistance gene as well as a fast-folding *sfGFP* gene. **(b)** Hierarchical clustering performed on correlations between each pair of reporter strain response at 1.87 μM malathion. **(c)** Average per cell *sfGFP* signal at 0.37 μM (left) and 1.83 μM (right) malathion normalized by signal at 0.0 μM malathion is shown for all 15 engineered strains. **(d)** Transfer curves (or response curves) for each strain is depicted with markers and their fit to Hill equation kinetics are given by solid lines. The Hill equation parameters are given in Table 1 The promoter sequences corresponding to each reporter and time points for each transfer curve are given in Supplementary Tables 2 and 4, respectively. The error bars represent the standard deviation from the mean across three biological replicates.

environmentally relevant way by sourcing malathion from the commonly used commercial insecticide called Spectracide (containing 50% malathion). First, it was verified that the response of the reporters to analytical standard malathion was consistent with the response when induced with Spectracide. That is to say that if the reporter was upregulated (downregulated) in response to malathion, it was also upregulated (downregulated) in response to Spectracide. Furthermore, the culture media containing nutrients and Spectracide that the reporter strains were cultured in was analyzed with mass spectrometry and compared

to the mass spectrum of analytical standard malathion. Comparing the two mass spectra, we found that they are nearly identical (Supplementary Figs. 7-19). See the Methods section for more details about the use of Spectracide as a source for malathion and Supplementary Figure 4 for the effect of Spectracide on the growth of the reporter strains.

To examine the transcriptional activity of *sfGFP*, controlled by the encoder gene promoters, cells are grown in in rich medium and fluorescence output was measured every three minutes over 24 hours of growth. This resulted in 400 time points per reporter strain, a nearly 45 fold increase over the number of time points obtained via RNA-seq. Prior to starting the experiment and collecting fluorescence measurements, reporter strains were induced with Spectracide to drive the reporter response. Since *sfGFP* is a stable protein with a long half-life and fast maturation time [78], the result is that each strain serves as a reporter for the rate of transcription initiation. This is distinctly different from the transcript abundance that is measured via RNA-seq due to the instability of mRNA molecules.

Inducing the reporter strains with malathion results in correlated transcriptional activity. To correlate the reporter strains' activity, first the *sfGFP* fluorescence is normalized by the OD to give average per cell fluorescence. The Pearson correlation between the average per cell fluorescence of all pairs of reporters is given in Figure 4b. From the heatmap, three distinct positively correlated clusters are apparent. The strains *cspA2*, *atpB*, *fabA*, *acrA*, and *petA* form the first cluster. The second positively correlated cluster contains *uncharacterized protein II*, *capB*, and *putative ABC transport system*. Lastly, *gltA*, *putative outer membrane porin A*, and *lpxC* form the third cluster. Moreover, we see that the first cluster negatively correlates with the second and that the second cluster negatively correlates with the third. The present correlations thus suggest that the genes within a cluster may have functional dependency in the presence of malathion or they share a transcriptional regulator. This also highlights the role of redundancy in gene expression and has been studied widely in the form of gene co-expression networks or regulons [44].

Examining the transcription initiation driven by malathion at distinct concentrations reveals detailed gene expression dynamics, dependencies of expression on malathion concentration, as well as the correlations. Firstly, the fold change (with respect to 0.0 μM malathion and referred to as the background) reveals oscillatory signals in several strains; the reporters *atpB*, *petA*, *cspA2*, and *acrA* each contain oscillations that are near in phase at 0.38 μM malathion (Figure 4c). As the concentration of malathion is increased, only *atpB* and *petA* appear to remain in phase while the signals of the other strains strongly increase. We also see that *anti-sigma 28 factor* and *rpoA* oscillate with lower frequency and that *anti-sigma 28 factor* hits a peak around 10 hours after induction while *rpoA* hits an anti-peak around 10 hours after induction. For the lower malathion concentration, *sucC* has a large lag time until transcriptional activation occurs, however there is a sharp decrease in the lag time at the higher concentration. The strains *acrA*, *gltA*, *putative outer membrane porin A*, *putative ABC transport system*, and *lpxC* consistently respond within minutes of malathion induction with *lpxC* being the reporter with highest signal over background and *acrA* the reporter with highest overall signal energy (area under the curve) in early times. Though *cspA2* was shown by the RNA-seq data to be repressed by malathion, we find that *cspA2* strain is consistently activated in the presence of malathion. Of the remaining repressed promoters, *uncharacterized protein II* is far more repressed in the presence of malathion across all concentrations tested.

The response curves of the reporter strains to malathion strongly resemble Michaelis-Menten enzyme-substrate kinetics. Such kinetics are characterized by exactly two parameters and mathematically described by Hill functions [63] (Methods). The first parameter is the Hill coefficient or cooperativity, n, which is a measure of how steep the response curve is. This is also denoted as a measure of ultrasensitivity. The second parameter, K_M, is the Michaelis constant and it is equal to the malathion concentration at which the response is half of its minimum value subtracted from its maximum value. Figure 4d shows the malathion response curves of each reporter strain at the time point with maximum fold change with respect to the 0 μM malathion condition. The solid line depicts the fit of a Hill function to the experimentally generated response curves and the parameters of each Hill function are given in Table 1. The response shown is the average fluorescence per cell obtained by normalizing the sfGFP signal by the optical density. See Supplementary Table 4 for the precise time points used here for each strain and see Methods for further details on parameter fitting.

We find that there is significant variation across the Hill coefficient, dynamic range, and Michaelis constant in the library of reporters. The Hill coefficient ranges from 1.1 to 21.6, and recalling that this parameter is a measure of sensitivity, the extremes depicted by a small slope in strain *fabA* and large slope in strain *sucC*, respectively. The dynamic range, measured as the difference between the maximum signal and the minimum signal, ranges from 80 to 1401 and is obtained by *sucC* and the repressed *uncharacterized protein II*, respectively. The Michaelis constant ranges from 0.2 to 1.5, depicted by the shift in malathion concentration at which half of the maximum signal is achieved from *fabA* and *cspA2*.

Overall, we find that each synthetic reporter, selected via our data-driven sensor placement framework, is capable of detecting malathion with distinct dynamic ranges and sensitivity. Moreover, we note that two of the selected reporters, *ABC transporter* and *acrA*, are membrane transporters and are not expected to be specific to malathion. The above two points motivate combining features from individual reporters to generate a single (virtual) reporter that enhances sensing capabilities. In what follows we demonstrate one approach to achieve such a task.

Superimposing the response of multiple sensors creates an enhanced virtual sensor.

The genetic reporters characterized in the previous section respond to malathion with distinct timescales, amplitudes, and frequencies, each acting as a unique report of the environmental context. However, as explained previously, not every reporter is expected to uniquely respond to malathion. Therefore, when testing for malathion in an environmental scenario, the conclusion given by individual reporters are expected to have a higher false positive rate than if the measurements were aggregated to form a single, combined sensor.

Recognizing the need to construct a multi-component sensor from the reporters in our synthetic promoter library, in this subsection we explore an approach for incorporating each unique temporal response to produce a desired output that provides more information than a single reporter alone. This application of the library views the synthetic reporters as genetic basis functions with fixed expressivity, comprising a single-input-single-output genetic network. Here the single input is malathion and the single output is a virtual sensor. As opposed to a biological sensor, a virtual sensor solely processes data originally gathered by the distinct biological sensors [79]. In our case, the 15 genetic reporters described in the previous section comprise the biological sensors and we aggregate the response measurements from

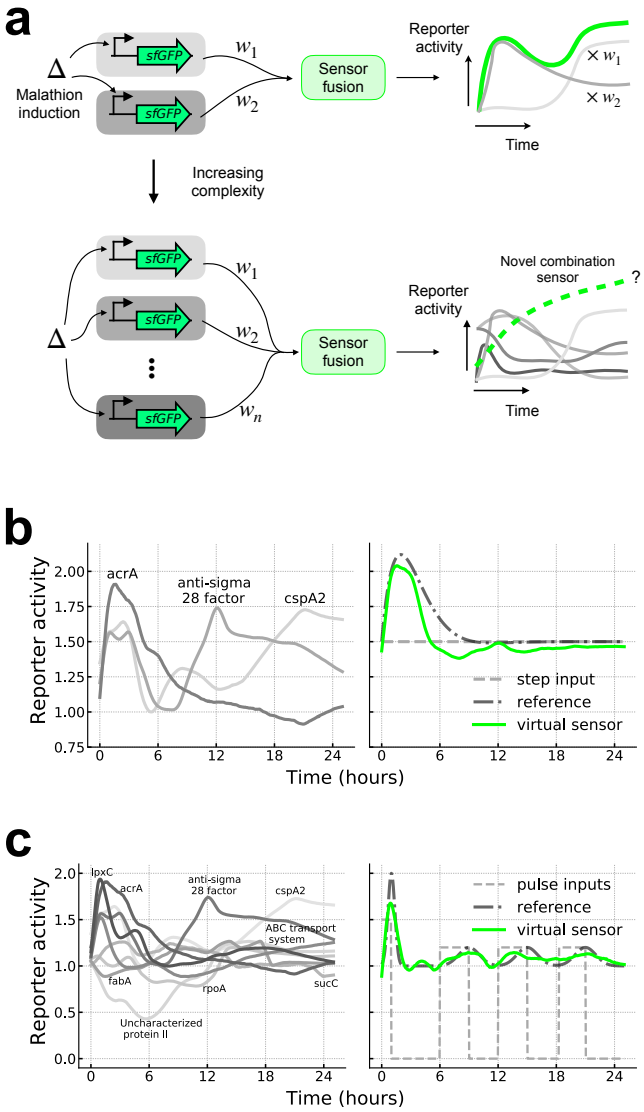

Figure 5: **The superposition of transcriptional genetic sensors creates a virtual, single-input, single-output genetic network.** **(a)** The schematic depicts the concept of virtual sensing, which combines the output of synthetic genetic sensors to produce a purely software-based output for enhanced malathion reporting. **(b)** The response of three reporters (left) are superimposed with weights $\{\beta_{acrA} = 0.6,\ \beta_{anti-sigma\ 28\ factor} = 0.31,\ \beta_{cspA2} = 0.26\}$ to output a virtual sensor which recapitulates the second-order response reference trajectory. The dotted blue line represents a step input of malathion, the solid orange curve depicts the desired reference response, and the dashed green curve is the weighted sum of the response to a step input of the three synthetic genetic sensors depicted on the left. **(c)** Nine reporters are superimposed with weights $\{\beta_{lpxC} = 0.5,\ \beta_{acrA} = 0.36,\ \beta_{fabA} = 0.11,\ \beta_{uncharacterized\ protein\ II} = 0.58,\ \beta_{rpoA} = 0.1,\ \beta_{anti-sigma\ 28\ factor} = 0.13,\ \beta_{ABC\ transport\ system} = 1.29,\ \beta_{cspA2} = 0.74,\ \beta_{sucC} = 0.32\}$ to recapitulate the sequence of radial basis function responses. See the caption of **(b)** for a description of the legend.

each to produce a purely virtual sensor that has a desired output (Figure 5a). Even though two of the malathion reporters, the membrane transporters, are expected to respond to an array of small molecules, virtual sensing can aggregate information from all sensors, increasing the confidence in the conclusion of the event that the sensors have been exposed to.

The usefulness of a virtual sensor in the setting of detection of a novel small compound is two-fold, i) aggregating contrasting responses can only reduce the false-positive rate of a detection event and ii) combining individual sensors in a software-based manner reduces the need for implementation of complex synthetic genetic networks and reduces metabolic burden on the host organism. Taking advantage of the benefits of virtual sensing, we develop an approach for enhancing malathion reporting by aggregating the response of the reporters in our library. Specifically, the weighted superposition of malathion responses are used to produce a desired output signal.

We show that transcriptional virtual sensing is capable of detecting environmentally relevant events. Consider a scenario where malathion is discarded in a prohibited site such as a body of water or soil. Such an event might trigger a reference (desired) response that resembles the response of a linear, second-order system to a step input [47]. Specifically, the reference response is characterized by a rapid response to malathion followed by lower magnitude, sustained response (Figure 5b). Treating the reporter library as genetic basis functions, we learn the sparse set of coefficients that approximate the reference trajectory (see Methods for details). We find that with only three sensors, the desired response is accurately captured. The strains *acrA*, *anti-sigma 28 factor*, and *cspA2* each possess peaks shortly after malathion induction, capturing the peak in the reference. At later times, the superposition of the three strains are able to recapitulate the sustained response.

We now consider a second scenario where we aim to detect malathion from a more subtle source where in pulses of malathion are introduced to the system periodically. Figure 5c depicts the pulse inputs and reference trajectory which is comprised of a linear combination of radial basis functions. We find that for this more complex scenario, superposition of the response of nine reporters is required to approximate the reference trajectory.

In both scenarios, a single genetic reporter would not be sufficient to inform of the type of event that occurred. Furthermore, we have shown how virtual sensing can prove useful for aggregation of measurements from individual sensors without having to clone synthetic multi-component reporters, a difficult task due to the tremendously large size of the design space and the emergent effects seen when composing genetic parts.

Detecting malathion in environmental samples.

In the previous section, we discussed how we can virtually enhance the sensing ability of the malathion reporter library in environmentally relevant scenarios. However, the library has only been examined in an ideal laboratory scenario with either pure or processed malathion that has been analyzed with mass spectrometry; it is not yet known if the reporters will be able to sense malathion when induced with actual environmental water samples that have been treated with the insecticide. Confounding factors may be present in the environmental sample such as other small compounds that may make it difficult to deconvolve malathion response from the response due to the confounder. Therefore, in this section we describe an experiment to assess whether or not the malathion concentration can be deduced from our reporters treated with environmental insecticide samples.

In order to test if the genetic reporters can sense malathion from environmental samples, irrigation water was collected from three crops after being sprayed with a mixture of Spectracide (50% malathion) and water (Figure 6a). The concentration of the mixture sprayed was either 0, 1, or 8 times the maximum recommended working concentration of Spectracide – 1 fluid ounce

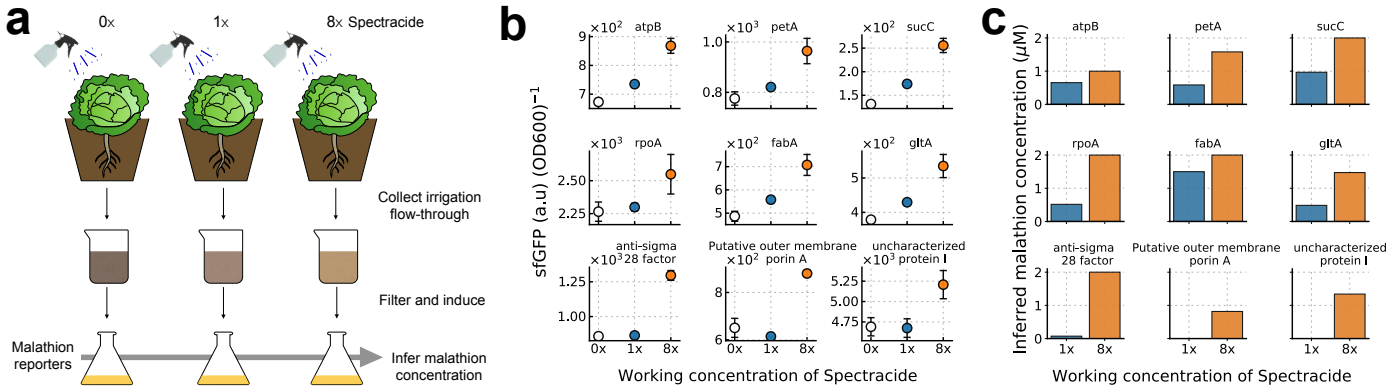

Figure 6: **Irrigation water containing malathion from an agricultural setting activates transcriptional reporters and allows for inference of environmental malathion concentration. (a)** Three cabbage plants are sprayed with a solution of 0, 1, and 8 times the working concentration of Spectracide, respectively. The flow-through is first captured and filtered and then used to induce transcriptional activity in the malathion reporter strains. Using previously characterized response curves for each reporter, an inference for the malathion concentration can be made. **(b)** The average per cell fluorescence (arbitrary units) of 9 out of the 15 malathon reporters, after 24 hours of induction, showed activation due to the soil runoff solution containing malathion. The working concentration of Spectracide is instructed as 1oz of Spectracide to 1 gallon of water. The error bars represent the sample standard deviation from the mean across three biological replicates. **(c)** The concentration of malathion present in the irrigation water is inferred using the signal from **(b)** and the fitted response curves from Figure 4d.

per gallon of water. To rid the solution of unwanted microbes and particles, the irrigation water was strained and filtered prior to to the induction of the genetic reporters (see Methods). The growth and induction protocols all remain the same as for the samples treated with Spectracide in Figure 4c,d.

We found that a total 9 out of the 15 of the reporters were activated by induction of the irrigation water containing malathion. Fig 6a shows the average per cell fluorescence 24 hours after induction of the nine strains subjected to 0, 1, or 8 times the working concentration of Spectracide. The reporters *atpB*, *petA*, *sucC*, *rpoA*, *fabA*, and *gltA* all show a response to malathion at 1x working concentration, while the remaining three did not show significant differences from the negative control in this range. Among the strains in Figure 6b, the strain *sucC* was activated the most, showing an 80% increase from the 0x to 8x condition after the 24 hour time period. This shows that many of the selected genetic reporters, 60%, are able to detect malathion in environmentally relevant scenarios, and, furthermore, we can use this data to infer the concentration of malathion present in the samples collected from the environment.

The response curves characterized previously in Figure 4d for each of the genetic reporters can be used to make an inference about the amount of malathion present in each environmental sample. Note that we are making the assumption that the response curves characterized for each of the nine reporters can be applied to this new setting of treatment with irrigation water. With this assumption we can then use the fitted Hill equations from Figure 4d and numerically estimate the malathion concentration that reproduces the signal at 1 or 8 times the working concentration of Spectracide. The results obtained are shown in Figure 6b for each of the nine strains. Through this approach, the reporters provide a range of inferred malathion concentrations; at the working concentration of Spectracide, we can infer that the concentration of malathion is in the range $0.48 - 0.97$ μM and at 8 times the working concentration of Spectracide, we can infer the concentration of malathion to be in the range $0.82 - 2$ μM. It is important to note that for most, if not all, of the characterized reporter strains, 2 μM was the maximum discernable concentration before the signal saturates. Therefore, it is possible the concentration of malathion is higher than 2 μM, however that range cannot be detected by our reporter library.

Discussion

It is often the case that biologists seek to identify key genes which show variation for the biological process of interest. Many tools have been developed or adapted to meet this need e.g. differential expression and principal component analysis to name only a few. However, when using the current tools, there is potential to measure system variables that are redundant which can lead to wasted time and resources. Therefore, we developed an efficient method that identifies the variables that allow for the inference of the complete system. The method combines dynamic mode decomposition (DMD) and observability of dynamical systems to provide a systematic approach for the discovery of perturbation-inducible genes. To extract optimal biosensors from our model, we showed that if the fold change was taken as the state of the system, the encoder genes inform the design of transcriptional reporters that showcase condition specific sensing.

We introduced DMD as a novel tool for analysis of transcriptome dynamics. In this case, we studied bulk transcriptome dynamics at the minutes resolution and showed that the low-dimensional DMD representation accurately predicts the dynamics and clusters genes based on temporal behavior. Our results suggest that DMD is a capable tool for analysis of transcriptomic data and warrants further exploration in single-cell RNA-seq and other 'omics technologies that aim to infer cell trajectories, pseudotime, and single-cell regulatory networks.

The identification of transcriptional genetic sensors was posed as a design challenge, where a subset of genes are selected to maximize the observability of the cell state. It was shown that a large fraction of genes contribute insignificantly to the cell state observability when only few time points are measured, further validating the common knowledge that genetic networks possess redundancies and are noisy. We also showed that it is significantly more beneficial to measure a sparse set of genes for more time points than to measure more genes for fewer time points.

Our results suggest future joint experimental and computational approaches which limit the amount of resources required to get a full description of the system dynamics. A natural extension of our work is to determine how well measurements from a small library of reporters recapitulate the bulk cell state under unseen conditions. Such studies will inform how RNA-seq data should be collected in the future in order to maximize the reconstruction accuracy and minimize labor and experimental costs.

The machine learning driven selection of genetic reporters was shown to produce 15 functional biosensors with a variety of malathion response curves. We demonstrated how to aggregate information from each reporter to create a virtual sensor that can be used to infer events of interest. Moreover, we showed that the genetic reporters can be used to detect malathion in environmental settings. More generally, our results and methodology offer an innovative approach that can be used to to identify perturbation-inducible gene expression systems. We emphasize that our approach takes advantage of the largely untapped resources present in native host genomes and we anticipate that techniques like the one developed here will produce a plethora of parts for synthetic biologists to build useful devices from.

Lastly, our developed approach makes no assumptions on the nature of the underlying system. In that sense, the framework we have developed is general and can be applied to data generated from other 'omics techniques and from any organism. In the case that a linear response model is insufficient for capturing the transcriptome dynamics, it can be extended to a variety of nonlinear models to capture nonlinear modes of response [71]. An interesting extension of observability to transcriptome dynamics would be to construct state-estimators (also known as observers) of the dynamics for real-time monitoring of gene interaction networks [80]. Such approaches could find potential use in designing and implementing better diagnostic tools for synthetic biologists. Finally, further refinement of the list of encoder genes could be obtained by fusing ChIP-seq (chromatin immunoprecipitation followed by sequencing) with RNA-seq measurements to discover transcription factors, however such an experimental assay can be prohibitively expensive. The DNA binding sites measured by ChIP-seq alone are not sufficient to infer regulation of transcription. However, together with RNA-seq, the set of encoder genes which causally drive the condition specific response can be uncovered.

Methods

Rapid culture sampling. For each biological replicate, *Pseudomonas fluorescens SBW25* glycerol stock was scraped and inoculated in 5 mL of fresh LB broth (Teknova Catalog no. L8022) and was incubated and shaken at 30°C and 200 r.p.m. for 15 hours. The OD_{600} of the 5 mL culture was measured and the entire culture was transferred to 50 mL of fresh LB broth, which was then proceeded by incubation and shaking. Once the OD_{600} of the 50 mL culture reached 0.5, the culture was again passaged into 300 mL of fresh LB broth. The 300 mL culture was grown until OD_{600} of 0.5. Then the culture was split into two 150 mL cultures (one for malathion induction and one for the negative control). The two cultures were sampled at evenly spaced intervals in time (see Supplementary Table 1 for sampling volumes and times) and after the 0 minute sample, malathion (Millipore Sigma Catalog no. 36143) was introduced to the positive condition at 1.83 mM. To separate the media from the cells, a vacuum manifold with 3D printed filter holders was constructed and utilized (Supplementary Figure 6). 0.45 μm PVDF membrane filters (Durapore Catalog no. HVLP04700) were placed on the filter holders, a vacuum pump was turned on, and the culture sample was dispensed onto the center of the filter, quickly separating the media from the cells. The filter with the cells was then placed into a 50 mL conical centrifuge tube (Fisher Scientific 1495949A) using sterile tweezers. The tube with the filter was then submerged into a liquid nitrogen bath for 10 seconds to flash freeze the sample. The sample were then stored -80 °C.

RNA extraction. To extract the RNA, first the filter-harvested cells were resuspended in 2 mL RNAprotect Bacterial Reagent (Qiagen Catalog no. 76506), then pelleted in a centrifuge. To lyse the cells, the pellet was then resuspended in 200 µL of TE Buffer containing 1 mg/mL lysozyme. The RNA was then extracted from the lysed cells using Qiagen RNeasy Mini Kit (Catalog no. 74104), and the samples were DNase treated and concentrated using Zymo RNA Clean and Concentrator (Catalog no. R1019).

RNA library preparation and sequencing. Bacterial rRNA was depleted using NEBNext Bacterial rRNA Depletion Kit (Catalog no. E7850X). The indexed cDNA library was generated using NEBNext Ultra II Directional RNA Library Prep (Catalog no. E7765L) and NEBNext Multiplex Oligos for Illumina (Catalog no. E6609S). In total, 40 samples (two biological replicates, 10 time points, two conditions) were prepped and sequenced. The library was sequenced at the Genetics Core in the Biological Nanostructures Laboratory at the University of California, Santa Barbara on an Illumina NextSeq with High Output, 150 Cycle, paired end settings.

Pre-processing of sequencing data. The raw reads were trimmed for adapters and quality using `Trimmomatic` [81]. The reads were then pseudoaligned with `Kallisto` [82] to the *Pseudomonas fluorescens SBW25* transcriptome generated using `GFFRead` [83] and GenBank genome AM181176.4. The normalized gene expression of transcripts per million (TPM), which takes into account sequencing depth and gene length, are used for modeling and analysis. Genes with an average TPM less than 100 in all experimental conditions were discarded from our analysis.

Malathion reporter library cloning. For the reporter plasmid cassette design, first, the closest intergenic region to the gene target larger than 100 base pairs (bp) was identified based on the open reading frame of the sequenced genome of *Pseudomonas fluorescens* SBW25 (GenBank genome AM181176.4). Primers were designed to include the entire intergenic region in order to capture any transcription-regulator binding sites surrounding the promoter (Figure 4a). The identified intergenic regions were amplified using the primers and this is what we refer to as 'promoter regions' following the terminology of [84]. The promoter regions were cloned into a cassette on the plasmid backbone pBHVK (Supplementary Figure 3) containing a bicistronic ribosome binding site and super folder GFP (*sfGFP*) as the reporter gene. Lastly, a cloning site was placed in the cassette so that the cloned promoter controls transcriptional activity of *sfGFP*.

The promoters were assembled onto the plasmid backbone pBHVK (see Supplementary Fig. 3) via Golden Gate Assembly [85] using NEB Golden Gate Assembly Kit (Catalog no. E1601S). Because of the potential of arcing during electrotransformation of *Pseudomonas fluorescens SBW25* with Golden Gate reaction buffers, the plasmids are first subcloned into *E. coli Mach1* (Thermo Fisher Scientific Catalog no. C862003) following the manufacturer's protocol for chemical transformation. Between three and six colonies are selected for each strain and the reporter cassette was sent for sequencing at Eurofins Genomics. Then the plasmid DNA was prepared from cultures of transformed Mach1 cells using Qiagen Spin Miniprep Kit (Catalog no. 27106) followed by chemical transformation into *SBW25*. *SBW25* was made chemically competent by washing a culture at OD_{600} of 0.3 with a solution of 10% glycerol two times, then resuspending in 500 μL of 10% glycerol. The plasmid DNA is added to 80 μL of the cell suspension and kept at 4°C for 30 minutes, then the cells were electroporated with 1600 V, 200 Ω, and 25 μF. The cells were immediately resuspended in 300 μL of SOC Broth (Fischer Scientific Catalog No. MT46003CR), recovered for 2 hours at 30°C in a shaking incubator, and plated onto 1.5% LB Agar plates with 50 $\frac{\mu g}{mL}$ Kanamycin. Again, three to six colonies of each strain have their reporter cassette sequenced at Eurofins Genomics and simultaneously glycerol stocks of each colony is prepared for long term storage.

Photobleaching of Spectracide. Spectracide malathion insect spray concentrate (Spectracide Catalog no. 071121309006) was utilized as the environmentally relevant source of malathion for the reporter library testing and contains 50% malathion. Spectracide is an opaque liquid. We found that we can remove the opaque substances by photobleaching a 5% Spectracide solution (in LB) in a Synergy H1

plate reader (Biotek), at $30°C$ and 800 r.p.m. OD_{600} and fluorescence (excitation 485nm, emission 528nm) were measured every 3 minutes for 8 hours. To ensure malathion remained in solution after photobleaching, the mass spectrum was analyzed at the University of California, Santa Barbara Mass Spectroscopy Facility. From this we determined that malathion is stable for the course of the photobleaching (Supplementary Figures 7 to 19).

Plate reader assays to measure response curves and doubling times. Scrapes of culture from glycerol stocks of each strain were used to inoculate 3 mL of LB (Kanamycin 50 $\frac{\mu g}{mL}$) in 10 mL 24 deep-well plate sealed with a breathable film (Spectrum Chemical Catalog no. 630-11763) and grown at $30°C$ overnight in a shaker incubator. The overnight cultures were diluted to an OD_{600} of 0.1 in 2 mL of LB and the cultures were grown for an additional 2 hours. 250 μL of this culture was then transferred to a 96 well optically-transparent microtiter plate. Photobleached spectracide (50% malathion) is then introduced (if relevant) to the cultures in the wells to give the desired concentration of malathion, and grown in a Synergy H1 plate reader (Biotek), at $30°C$ and 800 r.p.m. OD_{600} and *sfGFP* (excitation 485nm, emission 528nm) was measured every 3 minutes for 48 hours. Each data point in a response curve was generated by normalizing the *sfGFP* signal (arbitrary fluorescence units) by the OD_{600} to give the average per cell fluorescence, and only the data points before cell death (due to nutrient depletion or media evaporation) are used. The strain growth rates were calculated as $\ln(\text{initial } OD_{600}/\text{final } OD_{600})/(t_{\text{final}} - t_{\text{initial}})$, where the initial OD_{600} is the first measurement within the exponential phase and final OD_{600} is the last measurement within the exponential phase. Then the strain doubling times were calculated as $\ln(2)$ divided by the growth rate.

Collection and cleanup of irrigation water treated with Spectracide. Three cabbage plants were each potted in 5 gallon buckets with fresh soil (Harvest supreme) and a water catchment tray was placed under the plants to catch flow through. The first plant was sprayed with water containing no malathion and the flow through was collected in a 1 L pyrex bottle. The second plant was sprayed with a Spectracide (50% malathion) solution at a concentration of 1 fluid ounce per of gallon water – the maximum working concentration of Spectracide as recommended by the manufacturer. Lastly, the third plant was sprayed with the solution at 8 fluid ounces per gallon of water. Each plant was sprayed for one minute and the collected flow through from each plant were first strained using a 40 μm cell strainer (VWR 76327-098) to remove large microorganisms and large particles. The strained samples were then centrifuged to separate dense, soil particles from the Spectracide solution. Finally, the supernatant was vacuum filtered through a 0.22 μm membrane before induction of the reporters. The protocol for induction of the reporters with the irrigation water is the same as above.

Computing the dynamic mode decomposition. We now discuss the details of applying dynamic mode decomposition (DMD) to time-series data obtained from sequencing. As mentioned previously, many algorithms have been developed to compute the DMD modes, eigenvalues, and amplitudes, and a key requirement of almost all of the techniques is that the time points are spaced uniformly in time. In our work we begin by collecting the data for a single experimental condition into a time-ordered matrix, $\mathbf{X}$, which contains a total of $m \times r$ data snapshots for a data set with m time points and r replicates. For response to malathion, each $\mathbf{x}_i^{(j)}$ corresponds to the gene expression vector at time i in replicate j and is in the $((i+m) \times j)$th column of the data matrix $\mathbf{X}$ where $i \in \{0, 1, \ldots, m-1\}$ and $j \in \{1, 2, \ldots, r\}$. For gene expression data obtained from RNA-seq, each data snapshot typically contains thousands of rows denoted by n. The $n \times rm$ data matrix for the response to malathion is then given by

$$\mathbf{X}_{\text{malathion}} = \begin{bmatrix} | & | & & | & | & & | & \\ \mathbf{x}_0^{(1)} & \mathbf{x}_1^{(1)} & \ldots & \mathbf{x}_{m-1}^{(1)} & \mathbf{x}_0^{(2)} & \ldots & \mathbf{x}_{m-1}^{(2)} & \ldots \\ | & | & & | & | & & | & \end{bmatrix} \tag{1}$$

where each $\mathbf{x}_i \in \mathbb{R}^n$ represents the gene expression given in transcripts per million (TPM) from the malathion condition. Similarly, the data matrix for the control condition is constructed. The fold change data matrix, $\mathbf{Z}$, is subsequently computed as $\mathbf{Z} = \mathbf{X}_{\text{malathion}} \oslash \mathbf{X}_{\text{control}}$, where $\oslash$ denotes the Hadamard (element-wise) division of two matrices. Next we compute the mean-subtracted and standard deviation-normalized data matrix $\bar{\mathbf{Z}}$

$$\bar{\mathbf{Z}} = \begin{bmatrix} \dfrac{\mathbf{z}_0 - \boldsymbol{\mu}_{0:m-1}}{\boldsymbol{\sigma}^2_{0:m-1}} & \dfrac{\mathbf{z}_1 - \boldsymbol{\mu}_{0:m-1}}{\boldsymbol{\sigma}^2_{0:m-1}} & \ldots & \dfrac{\mathbf{z}_{m-1} - \boldsymbol{\mu}_{0:m-1}}{\boldsymbol{\sigma}^2_{0:m-1}} \end{bmatrix} \tag{2}$$

where $\boldsymbol{\mu}_{0:m-1}$ is the vector of time-averages of each gene and $\boldsymbol{\sigma}^2_{0:m-1}$ is the vector of time-standard deviations of each gene. The divisions in Eq. (2) are performed element-wise. We see that $\hat{\mathbf{Z}}$ is obtained by removing the time-averages from each gene and standardizing the time-variances of each gene. The mean subtraction operation is motivated by the fact that the mean of the data corresponds to the eigenvalue $\lambda = 1$, which is always an eigenvalue of the Koopman operator, the operator that DMD ultimately aims to approximate [86], and not one we are particularly interested in. The normalization by the standard deviation is performed so that the magnitude of the fold change has no implication on the connectivity of the learned dynamical system.

The algorithm we make use of to compute the dynamic mode decomposition (and the approximation of the Koopman operator) is exact DMD [50], which aims to identify the best-fit linear relationship between the following time-shifted data matrices

$$\bar{\mathbf{Z}}_p = \begin{bmatrix} \bar{\mathbf{z}}_0 & \bar{\mathbf{z}}_1 & \ldots & \bar{\mathbf{z}}_{m-2} \end{bmatrix}, \qquad \bar{\mathbf{Z}}_f = \begin{bmatrix} \bar{\mathbf{z}}_1 & \bar{\mathbf{z}}_2 & \ldots & \bar{\mathbf{z}}_{m-1} \end{bmatrix}$$

such that

$$\bar{\mathbf{Z}}_f = \mathbf{K}\bar{\mathbf{Z}}_p + \mathbf{r} \tag{3}$$

where $\mathbf{r}$ is the residual due to $\mathbf{K}$ only providing an approximation of the actual dynamics. Note that there are n^2 unknown parameters in $\mathbf{K}$ and $n \times m$ equations in Eq. (3). The residual is then minimized by Exact DMD (in the least squares sense) by first considering the reduced singular value decomposition (SVD) of $\hat{\mathbf{Z}}_p = \mathbf{U}\boldsymbol{\Sigma}\mathbf{W}^\top$ where $\boldsymbol{\Sigma} \in \mathbb{R}^{k \times k}$. As the number of time points, m, obtained from sequencing is typically much less than the number of genes, n, we keep $k \leq m$ singular values. Recognizing that minimizing the residual requires it to be orthogonal to the left singular vectors, we can pre-multiply (3) with $\mathbf{U}^\top$ to obtain

$$\mathbf{U}^\top \bar{\mathbf{Z}}_f = \mathbf{K}\mathbf{U}\boldsymbol{\Sigma}\mathbf{W}^\top. \tag{4}$$

Rearranging the above equation, it is shown that $\mathbf{K}$ is related to $\hat{\mathbf{K}}$ through a similarity transformation as shown in Eq. (5)

$$\hat{\mathbf{K}} = \mathbf{U}^\top \bar{\mathbf{Z}}_f \mathbf{W}\boldsymbol{\Sigma}^{-1} = \mathbf{U}^\top \mathbf{K}\mathbf{U} \tag{5}$$

meaning that the eigenvalues of $\hat{\mathbf{K}}$, λ, are equivalent to the k leading eigenvalues of $\mathbf{K}$ while the eigenvectors of $\hat{\mathbf{K}}$, $\mathbf{s}$, are related to the k leading eigenvectors of $\mathbf{K}$, $\mathbf{v}$, by $\mathbf{v} = \mathbf{U}\mathbf{s}$. This eigendecomposition then allows the fold change response to be written as the following spectral decomposition

$$\hat{\mathbf{z}}_i = \sum_{j=1}^{k} \mathbf{v}_j \lambda_j^i \mathbf{b}_j = \mathbf{V}\boldsymbol{\Lambda}^i \mathbf{b} \tag{6}$$

where $\mathbf{V}$ is a matrix whose columns are the eigenvectors (DMD modes) $\mathbf{v}_j$, and $\mathbf{b}$ is a vector of amplitudes corresponding to the gene expression at the initial time point as $\mathbf{b} = \mathbf{V}^\dagger \hat{\mathbf{z}}_0$. Here $\dagger$ represents the Moore-Penrose pseudoinverse of a matrix.

Using the above spectral decomposition, the modes can then be evolved in time for $m-1$ time steps to reconstruct the data from knowledge of the initial condition. Evolving past the mth time point allows for forecasting of the fold change response. To measure the accuracy of reconstruction we use the coefficient of determination

$$R^2 = 1 - \frac{\sum_{i=0}^{m} (\hat{\mathbf{z}}_i - \tilde{\mathbf{z}}_i)}{\sum_{i=0}^{m} (\hat{\mathbf{z}}_i - \bar{\mathbf{z}})} \tag{7}$$

where $\bar{\mathbf{z}}$ is the vector of each gene's mean expression, formally $\bar{z}^{(j)} = \sum_{k=0}^{m} \hat{z}_k^{(j)}$, and $\tilde{\mathbf{z}}_k = \mathbf{K}^k \hat{\mathbf{z}}_0$ is the prediction of $\hat{\mathbf{z}}_k$ given by the model starting from the initial condition.

Computing the gene sampling weights. Here we describe our methodology for ranking genes based on their contribution to the observability of the dynamical system learned via dynamic mode decomposition. We start by introducing the energy of a signal in discrete-time as

$$E_y = \sum_{i=0}^{\infty} \mathbf{y}_i^\top \mathbf{y}_i \tag{8}$$

which is closely related to the idea of energy in the physical sense and where $\mathbf{y} = \mathbf{W}\bar{\mathbf{z}}$ are measurements of the system state and $\mathbf{W} \in$

$\mathbb{R}^{p\times n}$. Rewriting the signal energy (8) using the recursion for $\mathbf{y}$ given as $\mathbf{y}_t = \mathbf{W}\mathbf{K}^t\bar{\mathbf{z}}_0$, we can reveal the connection between energy and observability

$$\begin{aligned} E_y &= \sum_{i=0}^{\infty} \bar{\mathbf{z}}_0^\top {\mathbf{K}^i}^\top \mathbf{W}^\top \mathbf{W}\mathbf{K}^i \bar{\mathbf{z}}_0 \\ &= \bar{\mathbf{z}}_0^\top (\sum_{i=0}^{\infty} {\mathbf{K}^i}^\top \mathbf{W}^\top \mathbf{W}\mathbf{K}^i)\bar{\mathbf{z}}_0 \\ &= \bar{\mathbf{z}}_0^\top \mathcal{X}_o \bar{\mathbf{z}}_0 \end{aligned} \tag{9}$$

where $\mathcal{X}_o$ is the infinite-horizon observability gramian, a symmetric matrix that is unique if the eigenvalues of $\mathbf{K}$ all have magnitude less than 1. The observability gramian describes how much gain will be attained by a system's output, $\mathbf{y}$, given an initial condition $\bar{\mathbf{z}}_0$. It simultaneously gives a measure of how well the initial condition $\bar{\mathbf{z}}_0$ can be estimated given only measurements of the system state y [75].

We use the observability gramian along with the measure of energy it provides to optimize for the gene sampling weights in the rows of $\mathbf{W}$ that maximize the signal energy E_y. Formally, the objective function is given as

$$\begin{aligned} &\max_{\mathbf{W}\in\mathbb{R}^{p\times n}} \bar{\mathbf{z}}_0^\top \mathcal{X}_o \bar{\mathbf{z}}_0 \\ &\text{subject to } \mathbf{W}\mathbf{W}^\top = I_{p\times p}. \end{aligned} \tag{10}$$

where we seek the matrix $\mathbf{W}$ that maximizes the observability of the cell state $\bar{\mathbf{z}}_0$. The constraint above enforces the following three points, i) the length of each row vector in $\mathbf{W}$ is not important, we are only concerned with the direction and the constraint sets the length of each row vector to be equal to 1, ii) the maximization problem is well-posed, i.e. the objective cannot blow up to infinity with the length constraint, and iii) the rows of $\mathbf{W}$ form p vectors of an orthonormal basis for $\mathbb{R}^p$, i.e. $\mathbf{W}\mathbf{W}^\top = I_{p\times p}$. Each row vector in $\mathbf{W}$ can then be viewed as a set of weights, each orthogonal to one another, that rank genes based on their contribution to the observability of the system. The optimization problem (10) represents a quadratic program with linear constraints, and the rows of $\mathbf{W}$ which maximize the objective are the p eigenvectors corresponding to the p eigenvalues with highest magnitude of the Gram matrix

$$\mathbf{G} = \sum_{i=0}^{\infty} \mathbf{K}^i \bar{\mathbf{z}}_0 \bar{\mathbf{z}}_0^\top {\mathbf{K}^i}^\top. \tag{11}$$

Since $\mathbf{G} \in \mathbb{R}^{n\times n}$ is a sum of quadratic forms, the result is that $\mathbf{G}$ has non-negative, real-valued eigenvalues. If the eigendecomposition is $\mathbf{G} = \mathbf{Q}\mathbf{D}\mathbf{Q}^{-1}$, then the solution to the optimization problem Eq. (10) is

$$\mathbf{W} = \begin{bmatrix} \mathbf{q}_1^\top \\ \vdots \\ \mathbf{q}_p^\top \end{bmatrix} \tag{12}$$

where $\mathbf{q}_1$ through $\mathbf{q}_p$ are the top eigenvectors of the Gram matrix $\mathbf{G}$. The proof of the solution to the optimization problem is provided in the Supplementary Information. The single set of gene sampling weights that maximize the observability are precisely $\mathbf{q}_1$ and from here on out we call these weights $\mathbf{w}$.

Since transcriptomic data sets typically have few initial conditions, i.e. biological and technical replicates, before solving for $\mathbf{w}$ we enrich our data set with N synthetic initial conditions that are randomly sampled as $Uniform(\min(\bar{\mathbf{z}}_0^{(j)}), \max(\bar{\mathbf{z}}_0^{(j)}))$ where j in $\{1, 2, ..., r\}$ and r is the number of replicates. The motivation for the artificial data generation is given in [87], where it is shown that artificially generated data points improved the estimate of the DMD model when the data set is affected by noise. N is chosen to be equal to the number of genes to ensure the matrix of initial conditions has full rank. Another issue that we have addressed are the instabilities present in the DMD eigenvalues. Consequently, the observability gramian is not unique and the sum in Eq. (11) diverges to infinity. To mend this issue, we compute the finite-horizon Gram matrix, where the sum in Eq. (9) and Eq. (11) is from 0 to m. This allows for the computation of the finite-horizon signal energy from Eq. (9) where the bounds on the sum are now from $i = 0$ to $i = m$.

Once $\mathbf{w}$ is obtained by solving Eq. (10), then measurements y_t, for t in $\{0, 1, ..., T\}$, are generated from $y_t = \mathbf{w}^\top \mathbf{K}^t \bar{\mathbf{z}}_0$ while keeping only the q elements of $\mathbf{w}$ with largest magnitude as nonzero. All other elements of $\mathbf{w}$ are set to zero to simulate the sampling of only selected genes. To reconstruct $\bar{\mathbf{z}}_0$ using only the measurements, we form the following observability matrix from the known sampling weights, $\mathbf{w}$ and the dynamics matrix $\mathbf{K}$

$$\begin{bmatrix} y_0 \\ y_1 \\ y_2 \\ \vdots \\ y_T \end{bmatrix} = \begin{bmatrix} \mathbf{w}^\top \\ \mathbf{w}^\top\mathbf{K} \\ \mathbf{w}^\top\mathbf{K}^2 \\ \vdots \\ \mathbf{w}^\top\mathbf{K}^T \end{bmatrix} \bar{\mathbf{z}}_\mathbf{0} = \mathcal{O}_T \bar{\mathbf{z}}_\mathbf{0} \tag{13}$$

and using the Moore-Penrose pseudoinverse we can obtain an estimate of the initial condition as follows

$$\mathcal{O}_T^\dagger \begin{bmatrix} y_0 \\ y_1 \\ y_2 \\ \vdots \\ y_T \end{bmatrix} = \hat{\mathbf{z}}_0 \approx \bar{\mathbf{z}}_0. \tag{14}$$

Increasing q while keeping T constant results in increasing reconstruction accuracy until a critical value of q such that the reconstruction accuracy plateaus; a similar scenario holds for keeping q constant and increasing T. When both T and q surpass the critical values, perfect reconstruction may be achieved.

When the computation of the Gram matrix, $\mathbf{G}$, is not computationally feasible, as can be the case when the dimensionality of the data are relatively high compared to that of bacterial transcription networks that we are dealing with here, the reduced order dynamics given by DMD can be used to compute an approximation to the leading eigenvalues and eigenvectors. The reduced order $\mathbf{G}$ is then given by

$$\tilde{\mathbf{G}} = \sum_{i=0}^{\infty} \hat{\mathbf{K}}^i \mathbf{U}^\top \bar{\mathbf{z}}_0 \bar{\mathbf{z}}_0^\top \mathbf{U} {\hat{\mathbf{K}}^i}^\top \tag{15}$$

where $\hat{\mathbf{K}}$ and $\mathbf{U}$ are given in Eq. (5). Supplementary Figure 2 shows the approximation of the leading eigenvalues and eigenvectors of $\mathbf{G}$ by $\tilde{\mathbf{G}}$.

Fitting the response curves to Hill kinetics. The malathion response curves for each sensor were fit to Hill functions of the form

$$y = y_{\min} + (y_{\max} - y_{\min})\frac{u^n}{K_M + u^n} = H_{\text{act}}(u) \tag{16}$$

for activated sensors and

$$y = y_{\max} - (y_{\max} - y_{\min})\frac{u^n}{K_M + u^n} = H_{\text{rep}}(u) \tag{17}$$

for repressed sensors. The parameter n is a measure of ultrasensitivity [88] or how steep the response curve is and is known as the Hill coefficient. The Michaelis constant, K_M, is equivalent to the malathion concentration at which the sensor response, y (measured in OD normalized arbitrary fluorescence units), is half of $(y_{\max} - y_{\min})$. The input u represents the malathion concentration in millimolar.

The objective function used to determine the parameters of the Hill equations is shown below

$$\min_{c, K_M} \sum_{(i=1)}^{n_c} (y_i - H(u_i))^2 \tag{18}$$

where H is the Hill function of the activator or repressor and n_c is the number of data points and is equivalent to the number of malathion concentrations times the number of replicates. The Levenberg-Marquadt algorithm is used to solve a nonlinear least squares problem to obtain a solution to optimization problem (18).

Approximating reference curves with genetic basis functions. Here we describe the treatment of the transcriptional sensors as genetic basis functions and how to use them to approximate reference curves. For this task, we work with the mean fold change of malathion response at 2.24 mM with respect to the zero malathion condition. The mean is taken across biological replicates for each of the n_s reporters: OD normalized arbitrary fluorescence units (which can alternatively be viewed as average per cell fluorescence). We start by collecting the

mean fold change response of each sensor at a particular instant in time, $\bar{\mathbf{y}}_i$, into a $n_s \times M$ data matrix, $\mathbf{Y}$

$$\mathbf{Y} = \begin{bmatrix} | & | & & | \\ \bar{\mathbf{y}}_0 & \bar{\mathbf{y}}_1 & \cdots & \bar{\mathbf{y}}_{M-1} \\ | & | & & | \end{bmatrix} \tag{19}$$

where M denotes the number of time points. Then a desired response vector, $\mathbf{s}$, is generated corresponding to the desired reference trajectory. For example, the first reference trajectory (Figure 5) used in this work is generated by

$$s_1(t) = 1.5 + 2.43e^{-0.44t} \sin 0.33t \tag{20}$$

which corresponds to a second-order underdamped system subject to a step input of 1.5 (arbitrary units). The second reference trajectory is generated by the superposition of radial basis functions

$$s_2(t) = e^{-\frac{(t-1)}{0.5}^2} + 0.2(e^{-\frac{(t-9)}{1.5}^2} + e^{-\frac{(t-15)}{1.5}^2} + e^{-\frac{(t-21)}{1.5}^2}) + 1. \tag{21}$$

The two functions were sampled at the time points corresponding to the sensor response measurements to obtain the vector $\mathbf{s}$.

Attending to realistic constraints surrounding genetic circuit design, data acquisition, and cost, we seek to identify the fewest combination of transcriptional sensors that can be used to recapitulate the desired response $\mathbf{s}$. This can be described mathematically using the following cost function

$$\min_{\beta \in \mathbb{R}^{n_s}_{\geq 0}} ||\mathbf{s} - \boldsymbol{\beta}^\top \mathbf{Y}||_2^2 + \gamma ||\boldsymbol{\beta}||_1 \tag{22}$$

where $||\bullet||_2$ is the Euclidean norm, quantifying the distance of a vector from the origin. The term $||\boldsymbol{\beta}||_1$ is the 1-norm and adding this quantity to the cost function has been shown to promote sparsity in the minimizer [89]. As γ increases, the number of sensors to recapitulate the desired response decreases. However if γ is too large, the sparse set of coefficients may be unable to accurately describe $\mathbf{s}$. This optimization problem represents a linear program with linear constraints and the minimizer is obtained using the splitting conic solver [90].

Data availability

The data generated from RNA sequencing are available at GEO Accession GSE200822: www.ncbi.nlm.nih.gov/geo/query/acc.cgi?acc=GSE200822. The DNA sequencing data for the reporter strains and the kinetic data generated from the spectrophotometer are available at: https://github.com/AqibHasnain/transcriptome-dynamics-dmd-observability.

Code availability

All codes used in this study are available at: https://github.com/AqibHasnain/transcriptome-dynamics-dmd-observability or available from the author's upon request.

Acknowledgments

This work was supported by DARPA, AFRL under contract numbers FA8750-17-C-0229, HR001117C0092, HR001117C0094, DEAC0576RL01830. Any opinions, findings, conclusions, or recommendations expressed in this material are those of the authors and do not necessarily reflect the views of the Defense Advanced Research Project Agency, the Department of Defense, or the United States government. This work was also funded, in part, by the Department of Energy's Biological and Environmental Research office, under the DOE Scientific Focus Area: Secure Biosystems Design project, via funding from Pacific Northwest National Laboratory subcontract numbers 545157 and 490521. This work received partially funding from the Army Young Investigator Award W911NF-20-1-0165 and the Army Research Office Grants W911NF-19-D-001, W911-NF-19-F-037, and W911-NF-19-0026. We acknowledge the use of the Biological Nanostructures Laboratory within the California NanoSystems Institute, supported by the University of California, Santa Barbara and the University of California, Office of the President. We thank Ryan Chambers, Trevor Marks, and Kirk Fields for construction of the vacuum manifold. We thank Jamiree Harrison for engaging in insightful discussions on linear systems theory.

Author contributions

A.H. and E.Y. designed research and experiments. A.H. performed experiments, performed formal analysis, analyzed data, and wrote the manuscript. S.B. assisted with RNA-seq sample collection and virtual sensor analysis. D.M.J. assisted with cloning of reporter strains; J.S. performed the mRNA library prep and sequencing; S.B.H. assisted in conceptualization and designing the time-series RNA-seq experiment; E.Y. supervised research and secured funding. A.H. revised the manuscript with inputs from all authors.

Competing interests

The authors declare no competing interests.

Bibliography

[1] Drew Endy. Foundations for engineering biology. *Nature*, 438(7067):449–453, 2005.

[2] Timothy S Gardner, Charles R Cantor, and James J Collins. Construction of a genetic toggle switch in escherichia coli. *Nature*, 403(6767):339–342, 2000.

[3] Michael B Elowitz and Stanislas Leibler. A synthetic oscillatory network of transcriptional regulators. *Nature*, 403(6767):335–338, 2000.

[4] Farren J Isaacs, Daniel J Dwyer, Chunming Ding, Dmitri D Pervouchine, Charles R Cantor, and James J Collins. Engineered riboregulators enable post-transcriptional control of gene expression. *Nature biotechnology*, 22(7):841–847, 2004.

[5] Travis S Bayer and Christina D Smolke. Programmable ligand-controlled riboregulators of eukaryotic gene expression. *Nature biotechnology*, 23(3):337–343, 2005.

[6] Amin Espah Borujeni, Dennis M Mishler, Jingzhi Wang, Walker Huso, and Howard M Salis. Automated physics-based design of synthetic riboswitches from diverse rna aptamers. *Nucleic acids research*, 44(1):1–13, 2016.

[7] Anselm Levskaya, Aaron A Chevalier, Jeffrey J Tabor, Zachary Booth Simpson, Laura A Lavery, Matthew Levy, Eric A Davidson, Alexander Scouras, Andrew D Ellington, Edward M Marcotte, et al. Engineering escherichia coli to see light. *Nature*, 438(7067):441–442, 2005.

[8] Jeong Wook Lee, Dokyun Na, Jong Myoung Park, Joungmin Lee, Sol Choi, and Sang Yup Lee. Systems metabolic engineering of microorganisms for natural and non-natural chemicals. *Nature chemical biology*, 8(6):536–546, 2012.

[9] William J Holtz and Jay D Keasling. Engineering static and dynamic control of synthetic pathways. *Cell*, 140(1):19–23, 2010.

[10] Ximing Li, Luna Rizik, Valeriia Kravchik, Maria Khoury, Netanel Korin, and Ramez Daniel. Synthetic neural-like computing in microbial consortia for pattern recognition. *Nature communications*, 12(1):1–12, 2021.

[11] D Ewen Cameron, Caleb J Bashor, and James J Collins. A brief history of synthetic biology. *Nature Reviews Microbiology*, 12(5):381–390, 2014.

[12] Adrian L Slusarczyk, Allen Lin, and Ron Weiss. Foundations for the design and implementation of synthetic genetic circuits. *Nature Reviews Genetics*, 13(6):406–420, 2012.

[13] Jeff Hasty, David McMillen, and James J Collins. Engineered gene circuits. *Nature*, 420(6912):224–230, 2002.

[14] Stanley Tabor and Charles C Richardson. A bacteriophage t7 rna polymerase/promoter system for controlled exclusive expression of specific genes. *Proceedings of the National Academy of Sciences*, 82(4):1074–1078, 1985.

[15] Heidi Redden, Nicholas Morse, and Hal S Alper. The synthetic biology toolbox for tuning gene expression in yeast. *FEMS yeast research*, 15(1):1–10, 2015.

[16] Rafael Silva-Rocha and Víctor de Lorenzo. Mining logic gates in prokaryotic transcriptional regulation networks. *FEBS letters*, 582(8):1237–1244, 2008.

[17] Goksel Mısırlı, Jennifer Hallinan, Matthew Pocock, Phillip Lord, James Alastair McLaughlin, Herbert Sauro, and Anil Wipat. Data integration and mining for synthetic biology design. *ACS synthetic biology*, 5(10):1086–1097, 2016.

[18] Ayaan Hossain, Eriberto Lopez, Sean M Halper, Daniel P Cetnar, Alexander C Reis, Devin Strickland, Eric Klavins, and Howard M Salis. Automated design of thousands of nonrepetitive parts for engineering stable genetic systems. *Nature biotechnology*, 38(12):1466–1475, 2020.

[19] Adam J Meyer, Thomas H Segall-Shapiro, Emerson Glassey, Jing Zhang, and Christopher A Voigt. Escherichia coli "marionette" strains with 12 highly optimized small-molecule sensors. *Nature chemical biology*, 15(2):196–204, 2019.

[20] Travis L La Fleur, Ayaan Hossain, and Howard M Salis. Automated model-predictive design of synthetic promoters to control transcriptional profiles in bacteria. *bioRxiv*, 2021.

[21] Alan Costello and Ahmed H Badran. Synthetic biological circuits within an orthogonal central dogma. *Trends in biotechnology*, 39(1):59–71, 2021.

[22] Mario A Marchisio and Jörg Stelling. Automatic design of digital synthetic gene circuits. *PLoS computational biology*, 7(2):e1001083, 2011.

[23] Alec AK Nielsen, Bryan S Der, Jonghyeon Shin, Prashant Vaidyanathan, Vanya Paralanov, Elizabeth A Strychalski, David Ross, Douglas Densmore, and Christopher A Voigt. Genetic circuit design automation. *Science*, 352(6281), 2016.

[24] Ye Chen, Shuyi Zhang, Eric M Young, Timothy S Jones, Douglas Densmore, and Christopher A Voigt. Genetic circuit design automation for yeast. *Nature Microbiology*, 5(11):1349–1360, 2020.

[25] Tobias Schladt, Nicolai Engelmann, Erik Kubaczka, Christian Hochberger, and Heinz Koeppl. Automated design of robust genetic circuits: Structural variants and parameter uncertainty. *ACS Synthetic Biology*, 2021.

[26] Christopher A Voigt. Genetic parts to program bacteria. *Current opinion in biotechnology*, 17(5):548–557, 2006.

[27] Luc Bousse. Whole cell biosensors. *Sensors and Actuators B: Chemical*, 34(1-3):270–275, 1996.

[28] Michael Moraskie, Harun Roshid, Gregory O'Connor, Emre Dikici, Jean-Marc Zingg, Sapna Deo, and Sylvia Daunert. Microbial whole-cell biosensors: Current applications, challenges, and future perspectives. *Biosensors and Bioelectronics*, page 113359, 2021.

[29] Yizhi Song, Cordelia PN Rampley, Xiaoyu Chen, Fawen Du, Ian P Thompson, and Wei E Huang. Application of bacterial whole-cell biosensors in health. *Handbook of Cell Biosensors*, pages 945–961, 2022.

[30] Howard Salis, Alvin Tamsir, and Christopher Voigt. Engineering bacterial signals and sensors. *Bacterial Sensing and Signaling*, 16:194–225, 2009.

[31] Baojun Wang, Mauricio Barahona, and Martin Buck. A modular cell-based biosensor using engineered genetic logic circuits to detect and integrate multiple environmental signals. *Biosensors and Bioelectronics*, 40(1):368–376, 2013.

[32] Huiqing Chong and Chi Bun Ching. Development of colorimetric-based whole-cell biosensor for organophosphorus compounds by engineering transcription regulator dmpr. *ACS synthetic biology*, 5(11):1290–1298, 2016.

[33] Brigitta Kurenbach, Delphine Marjoshi, Carlos F Amábile-Cuevas, Gayle C Ferguson, William Godsoe, Paddy Gibson, and Jack A Heinemann. Sublethal exposure to commercial formulations of the herbicides dicamba, 2, 4-dichlorophenoxyacetic acid, and glyphosate cause changes in antibiotic susceptibility in escherichia coli and salmonella enterica serovar typhimurium. *MBio*, 6(2):e00009–15, 2015.

[34] Eric VanArsdale, Chen-yu Tsao, Yi Liu, Chen-yu Chen, Gregory F Payne, and William E Bentley. Redox-based synthetic biology enables electrochemical detection of the herbicides dicamba and roundup via rewired escherichia coli. *ACS sensors*, 4(5):1180–1184, 2019.

[35] Yang-Chun Yong and Jian-Jiang Zhong. A genetically engineered whole-cell pigment-based bacterial biosensing system for quantification of n-butyryl homoserine lactone quorum sensing signal. *Biosensors and Bioelectronics*, 25(1):41–47, 2009.

[36] J Christopher Anderson, Elizabeth J Clarke, Adam P Arkin, and Christopher A Voigt. Environmentally controlled invasion of cancer cells by engineered bacteria. *Journal of molecular biology*, 355(4):619–627, 2006.

[37] Tal Danino, Arthur Prindle, Gabriel A Kwong, Matthew Skalak, Howard Li, Kaitlin Allen, Jeff Hasty, and Sangeeta N Bhatia. Programmable probiotics for detection of cancer in urine. *Science translational medicine*, 7(289):289ra84–289ra84, 2015.

[38] Xinyi Wan, Behide Saltepe, Luyang Yu, and Baojun Wang. Programming living sensors for environment, health and biomanufacturing. *Microbial biotechnology*, 2021.

[39] Michael I Love, Wolfgang Huber, and Simon Anders. Moderated estimation of fold change and dispersion for rna-seq data with deseq2. *Genome biology*, 15(12):1–21, 2014.

[40] Mark D Robinson, Davis J McCarthy, and Gordon K Smyth. edger: a bioconductor package for differential expression analysis of digital gene expression data. *Bioinformatics*, 26(1):139–140, 2010.

[41] Nicholas J Schurch, Pietá Schofield, Marek Gierliński, Christian Cole, Alexander Sherstnev, Vijender Singh, Nicola Wrobel, Karim Gharbi, Gordon G Simpson, Tom Owen-Hughes, et al. How many biological replicates are needed in an rna-seq experiment and which differential expression tool should you use? *Rna*, 22(6):839–851, 2016.

[42] Juliana Costa-Silva, Douglas Domingues, and Fabricio Martins Lopes. Rna-seq differential expression analysis: An extended review and a software tool. *PloS one*, 12(12):e0190152, 2017.

[43] Jonathan M Raser and Erin K O'shea. Noise in gene expression: origins, consequences, and control. *Science*, 309(5743):2010–2013, 2005.

[44] Sipko Van Dam, Urmo Vosa, Adriaan van der Graaf, Lude Franke, and Joao Pedro de Magalhaes. Gene co-expression analysis for functional classification and gene–disease predictions. *Briefings in bioinformatics*, 19(4):575–592, 2018.

[45] Brian DO Anderson and John B Moore. *Optimal filtering*. Courier Corporation, 2012.

[46] Donald J Chmielewski, Tasha Palmer, and Vasilios Manousiouthakis. On the theory of optimal sensor placement. *AIChE journal*, 48(5):1001–1012, 2002.

[47] Joao P Hespanha. *Linear systems theory*. Princeton university press, 2018.

[48] Peter J Schmid. Dynamic mode decomposition of numerical and experimental data. *Journal of fluid mechanics*, 656:5–28, 2010.

[49] Clarence W Rowley, Igor Mezic, Shervin Bagheri, Philipp Schlatter, Dans Henningson, et al. Spectral analysis of nonlinear flows. *Journal of fluid mechanics*, 641(1):115–127, 2009.

[50] Jonathan H Tu. *Dynamic mode decomposition: Theory and applications*. PhD thesis, Princeton University, 2013.

[51] Milena Anguelova. *Observability and identifiability of nonlinear systems with applications in biology*. Chalmers Tekniska Hogskola (Sweden), 2007.

[52] Aqib Hasnain, Nibodh Boddupalli, and Enoch Yeung. Optimal reporter placement in sparsely measured genetic networks using the koopman operator. In *2019 IEEE 58th Conference on Decision and Control (CDC)*, pages 19–24. IEEE, 2019.

[53] Peter Flessel, PJE Quintana, and Kim Hooper. Genetic toxicity of malathion: a review. *Environmental and molecular mutagenesis*, 22(1):7–17, 1993.

[54] WN Aldridge, JW Miles, DL Mount, and RD Verschoyle. The toxicological properties of impurities in malathion. *Archives of toxicology*, 42(2):95–106, 1978.

[55] I Desi, Gy Dura, L Gönczi, Zs Kneffel, A Strohmayer, and Z Szabo. Toxicity of malathion to mammals, aquatic organisms and tissue culture cells. *Archives of environmental contamination and toxicology*, 3(4):410–425, 1975.

[56] Jewell D Wilson. *Toxicological profile for malathion*. Agency for Toxic Substances and Disease Registry, 2003.

[57] Muhammad Syafrudin, Risky Ayu Kristanti, Adhi Yuniarto, Tony Hadibarata, Jongtae Rhee, Wedad A Al-Onazi, Tahani Saad Algarni, Abdulhadi H Almarri, and Amal M Al-Mohaimeed. Pesticides in drinking water—a review. *International Journal of Environmental Research and Public Health*, 18(2):468, 2021.

[58] Bryson D Bennett, Elizabeth H Kimball, Melissa Gao, Robin Osterhout, Stephen J Van Dien, and Joshua D Rabinowitz. Absolute metabolite concentrations and implied enzyme active site occupancy in escherichia coli. *Nature chemical biology*, 5(8):593–599, 2009.

[59] KayLynn Newhart. Environmental fate of malathion. *California Environmental Protection Agency*, 11:1–20, 2006.

[60] Robert W Jackson, Gail M Preston, and Paul B Rainey. Genetic characterization of pseudomonas fluorescens sbw25 rsp gene expression in the phytosphere and in vitro. *Journal of bacteriology*, 187(24):8477–8488, 2005.

[61] Ana Conesa, Pedro Madrigal, Sonia Tarazona, David Gomez-Cabrero, Alejandra Cervera, Andrew McPherson, Michał Wojciech Szcześniak, Daniel J Gaffney, Laura L Elo, Xuegong Zhang, et al. A survey of best practices for rna-seq data analysis. *Genome biology*, 17(1):1–19, 2016.

[62] Maurice Filo and Mustafa Khammash. A class of simple biomolecular antithetic proportional-integral-derivative controllers. *bioRxiv*, pages 2021–03, 2021.

[63] Uri Alon. *An introduction to systems biology: design principles of biological circuits*. CRC press, 2019.

[64] Bingni W Brunton, Lise A Johnson, Jeffrey G Ojemann, and J Nathan Kutz. Extracting spatial–temporal coherent patterns in large-scale neural recordings using dynamic mode decomposition. *Journal of neuroscience methods*, 258:1–15, 2016.

[65] Shara Balakrishnan, Aqib Hasnain, Nibodh Boddupalli, Dennis M Joshy, Robert G Egbert, and Enoch Yeung. Prediction of fitness in bacteria with causal jump dynamic mode decomposition. In *2020 American Control Conference (ACC)*, pages 3749–3756. IEEE, 2020.

[66] Lawrence Sirovich. A novel analysis of gene array data: yeast cell cycle. *Biology Methods and Protocols*, 5(1):bpaa018, 2020.

[67] Jake P Taylor-King, Asbjørn N Riseth, Will Macnair, and Manfred Claassen. Dynamic distribution decomposition for single-cell snapshot time series identifies subpopulations and trajectories during ipsc reprogramming. *PLoS computational biology*, 16(1):e1007491, 2020.

[68] Aqib Hasnain, Subhrajit Sinha, Yuval Dorfan, Amin Espah Borujeni, Yongjin Park, Paul Maschhoff, Uma Saxena, Joshua Urrutia, Niall Gaffney, Diveena Becker, et al. A data-driven method for quantifying the impact of a genetic circuit on its host. In *2019 IEEE Biomedical Circuits and Systems Conference (BioCAS)*, pages 1–4. IEEE, 2019.

[69] Orly Alter, Patrick O Brown, and David Botstein. Singular value decomposition for genome-wide expression data processing and modeling. *Proceedings of the National Academy of Sciences*, 97(18):10101–10106, 2000.

[70] Justin Tan, Anand V Sastry, Karoline S Fremming, Sara P Bjørn, Alexandra Hoffmeyer, Sangwoo Seo, Bjørn G Voldborg, and Bernhard O Palsson. Independent component analysis of e. coli's transcriptome reveals the cellular processes that respond to heterologous gene expression. *Metabolic Engineering*, 61:360–368, 2020.

[71] Enoch Yeung, Soumya Kundu, and Nathan Hodas. Learning deep neural network representations for koopman operators of nonlinear dynamical systems. In *2019 American Control Conference (ACC)*, pages 4832–4839. IEEE, 2019.

[72] Yang-Yu Liu, Jean-Jacques Slotine, and Albert-Laszlo Barabasi. Observability of complex systems. *Proceedings of the National Academy of Sciences*, 110(7):2460–2465, 2013.

[73] Didier Georges. The use of observability and controllability gramians or functions for optimal sensor and actuator location in finite-dimensional systems. In *Proceedings of 1995 34th ieee conference on decision and control*, volume 4, pages 3319–3324. IEEE, 1995.

[74] PC Müller and HI Weber. Analysis and optimization of certain qualities of controllability and observability for linear dynamical systems. *Automatica*, 8(3):237–246, 1972.

[75] Athanasios C Antoulas. *Approximation of large-scale dynamical systems*. SIAM, 2005.

[76] Jason Ernst, Oded Vainas, Christopher T Harbison, Itamar Simon, and Ziv Bar-Joseph. Reconstructing dynamic regulatory maps. *Molecular systems biology*, 3(1):74, 2007.

[77] The gene ontology resource: enriching a gold mine. *Nucleic Acids Research*, 49(D1):D325–D334, 2021.

[78] Anton Khmelinskii, Philipp J Keller, Anna Bartosik, Matthias Meurer, Joseph D Barry, Balca R Mardin, Andreas Kaufmann, Susanne Trautmann, Malte Wachsmuth, Gislene Pereira, et al. Tandem fluorescent protein timers for in vivo analysis of protein dynamics. *Nature biotechnology*, 30(7):708–714, 2012.

[79] Dominik Martin, Niklas Kühl, and Gerhard Satzger. Virtual sensors. *Business & Information Systems Engineering*, 63(3):315–323, 2021.

[80] Gabriele Lillacci and Mustafa Khammash. Parameter estimation and model selection in computational biology. *PLoS computational biology*, 6(3):e1000696, 2010.

[81] Anthony M Bolger, Marc Lohse, and Bjoern Usadel. Trimmomatic: a flexible trimmer for illumina sequence data. *Bioinformatics*, 30(15):2114–2120, 2014.

[82] Nicolas L Bray, Harold Pimentel, Páll Melsted, and Lior Pachter. Near-optimal probabilistic rna-seq quantification. *Nature biotechnology*, 34(5):525–527, 2016.

[83] Geo Pertea and Mihaela Pertea. Gff utilities: Gffread and gffcompare. *F1000Research*, 9, 2020.

[84] Alon Zaslaver, Anat Bren, Michal Ronen, Shalev Itzkovitz, Ilya Kikoin, Seagull Shavit, Wolfram Liebermeister, Michael G Surette, and Uri Alon. A comprehensive library of fluorescent transcriptional reporters for escherichia coli. *Nature methods*, 3(8):623–628, 2006.

[85] Carola Engler, Romy Kandzia, and Sylvestre Marillonnet. A one pot, one step, precision cloning method with high throughput capability. *PloS one*, 3(11):e3647, 2008.

[86] Igor Mezić. Spectral properties of dynamical systems, model reduction and decompositions. *Nonlinear Dynamics*, 41(1):309–325, 2005.

[87] Subhrajit Sinha, Bowen Huang, and Umesh Vaidya. On robust computation of koopman operator and prediction in random dynamical systems. *Journal of Nonlinear Science*, 30(5):2057–2090, 2020.

[88] Albert Goldbeter and Daniel E Koshland. An amplified sensitivity arising from covalent modification in biological systems. *Proceedings of the National Academy of Sciences*, 78(11):6840–6844, 1981.

[89] Robert Tibshirani. Regression shrinkage and selection via the lasso. *Journal of the Royal Statistical Society: Series B (Methodological)*, 58(1):267–288, 1996.

[90] Brendan O'donoghue, Eric Chu, Neal Parikh, and Stephen Boyd. Conic optimization via operator splitting and homogeneous self-dual embedding. *Journal of Optimization Theory and Applications*, 169(3):1042–1068, 2016.

Malathion reporter	Locus tag	Molecular function	Act./Rep.	y_{min}	y_{max}	K_M	n
atpB	PFLU_6124	• proton-transporting ATP synthase activity, rotational mechanism	Activated	1467	1783	0.6	4.5
petA	PFLU_0841	• 2 iron, 2 sulfur cluster binding, • metal ion binding • ubiquinol-cytochrome-c reductase activity	Activated	853	1125	1.4	2.4
sucC	PFLU_1823	• ATP binding • magnesium ion binding • succinate-CoA ligase activity	Activated	257	337	0.4	21.6
rpoA	PFLU_5502	• DNA binding • protein dimerization activity • DNA-directed 5'-3' RNA polymerase activity	Activated	1256	1542	0.9	3.0
fabA	PFLU_1836	• dehydratase activity • isomerase activity	Activated	292	373	0.2	1.1
anti-sigma 28 factor	PFLU_4736	• Negative regulator of flagellin synthesis	Activated	339	535	0.7	1.5
Uncharacterized protein I	PFLU_3761		Activated	2465	3110	0.5	2.7
cspA2	PFLU_4150	• major cold shock protein	Activated	706	1186	1.5	5.3
Putative ABC transport protein	PFLU_0376	• ligand-gated ion channel activity	Activated	584	1083	1.0	2.0
gltA	PFLU_1815	• citrate (Si)-synthase activity	Activated	238	458	0.9	1.9
lpxC	PFLU_0953	• metal ion binding • deacetylase activity	Activated	1017	2418	0.4	8.7
Uncharacterized protein II	PFLU_1358		Repressed	1073	3387	0.3	1.9
capB	PFLU_1302A	• cold shock protein	Repressed	9616	10543	1.0	8.6
Putative outer membrane porin A protein	PFLU_4612	• porin activity	Activated	642	1172	0.6	1.5
acrA	PFLU_1380	• transmembrane transporter activity	Activated	354	682	0.9	2.9

Table 1: Encoder library metadata and transfer curve parameters for the fitted Hill equations in Fig. 4d.

Learning transcriptome dynamics for discovery of optimal genetic reporters of novel compounds

Aqib Hasnain et al.

1 Supplementary Text

1.1 Observability maximization for transcriptome dynamics

Here we derive the solution to the observability maximization problem briefly outlined in the Methods section. Recall that we have a state-space representation of the transcriptome dynamics as

$$\begin{aligned} \mathbf{x}_{t+1} &= \mathbf{K}\mathbf{x}_t \\ \mathbf{y} &= \mathbf{W}\mathbf{x}_t \end{aligned} \tag{1}$$

where $\mathbf{x} \in \mathbb{R}^n$ is the (hidden) cell state, $\mathbf{K}$ is the state transition matrix, $\mathbf{W}$ are the unknown gene sampling weights, and $\mathbf{y} \in \mathbb{R}^p$ are the p measurements. The objective, $\mathcal{J}$, is formulated by the signal energy (or output energy) of the system

$$\mathcal{J} = \sum_{i=1}^{m} \mathbf{y}_i^\top \mathbf{y}_i = \sum_{i=0}^{m} \mathbf{x}_0^\top {\mathbf{K}^i}^\top \mathbf{W}^\top \mathbf{W}\mathbf{K}^i \mathbf{x}_0, \tag{2}$$

and we seek the gene sampling weights $\mathbf{W}$ which maximize the objective

$$\begin{aligned} &\max_{\mathbf{W}\in\mathbb{R}^{p\times n}} \mathcal{J} \\ &\text{subject to } \mathbf{W}\mathbf{W}^\top = I_{p\times p}. \end{aligned} \tag{3}$$

The constraint enforces that the rows of $\mathbf{W}$ are orthogonal to each other and that the length of each row be equal to 1. This further avoids the issue of the objective blowing up to infinity. The solution to the above optimization problem is obtained by forming the Lagrangian dual problem and finding the maxima of the the dual objective in terms of the dual variable (a $p \times p$ matrix), $\mathbf{D}$, i.e.

$$\begin{aligned} &\max_{\mathbf{W}\in\mathbb{R}^{p\times n}} \mathcal{J} + \mathcal{L} \\ &\text{where } \mathcal{L} = -\mathrm{tr}\Big((\mathbf{W}\mathbf{W}^\top - I_{p\times p})\mathbf{D}\Big) \end{aligned} \tag{4}$$

and tr() denotes the trace operator. Differentiating the dual objective with respect to $\mathbf{W}^\top$ and equating to 0, we have

$$\begin{aligned} \frac{\partial(\mathcal{J}+\mathcal{L})}{\partial \mathbf{W}^\top} &= \frac{\partial}{\partial \mathbf{W}^\top}\left(\sum_{i=0}^{m} \mathbf{x}_0^\top {\mathbf{K}^i}^\top \mathbf{W}^\top \mathbf{W}\mathbf{K}^i\mathbf{x}_0 - \mathrm{tr}\Big((\mathbf{W}\mathbf{W}^\top - I_{p\times p})\mathbf{D}\Big)\right) \\ &= \frac{\partial}{\partial \mathbf{W}^\top}\left(\sum_{i=0}^{m} \mathrm{tr}(\mathbf{x}_0^\top {\mathbf{K}^i}^\top \mathbf{W}^\top \mathbf{W}\mathbf{K}^i\mathbf{x}_0) - \mathrm{tr}\Big((\mathbf{W}\mathbf{W}^\top - I_{p\times p})\mathbf{D}\Big)\right) \\ &= \frac{\partial}{\partial \mathbf{W}^\top}\left(\sum_{i=0}^{m} \mathrm{tr}(\mathbf{W}\mathbf{K}^i\mathbf{x}_0\mathbf{x}_0^\top {\mathbf{K}^i}^\top \mathbf{W}^\top) - \mathrm{tr}\Big((\mathbf{W}\mathbf{W}^\top - I_{p\times p})\mathbf{D}\Big)\right) \\ &= \frac{\partial}{\partial \mathbf{W}^\top}\left(\sum_{i=0}^{m} \mathrm{tr}(\mathbf{W}\mathbf{G}^{(i)}\mathbf{W}^\top) - \mathrm{tr}\Big((\mathbf{W}\mathbf{W}^\top - I_{p\times p})\mathbf{D}\Big)\right) \\ &= \frac{\partial}{\partial \mathbf{W}^\top}\left(\mathrm{tr}(\mathbf{W}\sum_{i=0}^{m} \mathbf{G}^{(i)}\mathbf{W}^\top) - \mathrm{tr}\Big((\mathbf{W}\mathbf{W}^\top - I_{p\times p})\mathbf{D}\Big)\right) \\ &= \frac{\partial}{\partial \mathbf{W}^\top}\left(\mathrm{tr}(\mathbf{W}\mathbf{G}\mathbf{W}^\top) - \mathrm{tr}\Big((\mathbf{W}\mathbf{W}^\top - I_{p\times p})\mathbf{D}\Big)\right) \\ &= 2\mathbf{G}\mathbf{W}^\top - 2\mathbf{W}^\top\mathbf{D} = 0 \end{aligned} \tag{5}$$

where the second equality comes from the fact that $\mathcal{J}$ is a sum of m scalars and so applying the trace operator has no effect on the sum, the third equality uses the cyclic property of the trace of products, and the fifth equality uses the fact that $\mathrm{tr}(\mathbf{A}) + \mathrm{tr}(\mathbf{B}) = \mathrm{tr}(\mathbf{A} + \mathbf{B})$. Finally, the Gram matrix, $\mathbf{G}$, is defined to be $\mathbf{G} = \sum_i \mathbf{G}^{(i)} = \sum_i \mathbf{K}^i \mathbf{x}_0 \mathbf{x}_0^\top \mathbf{K}^{i^\top}$, a sum of quadratic forms, which is itself a quadratic form and therefore a symmetric matrix with non-negative, real-valued eigenvalues. From the final equality in Eq. (5) we have

$$\mathbf{G}\mathbf{W}^\top = \mathbf{W}^\top \mathbf{D} \tag{6}$$

which says columns of the eigenvectors of $\mathbf{G}$ are the rows of gene sampling weights $\mathbf{W}$. Moreover, the eigenvector of $\mathbf{G}$ corresponding to the eigenvalue with largest magnitude in $\mathbf{D}$ is the maximizer when $p = 1$.

1.2 Fold change dynamics of two linear systems

We have reasoned in the main text that the gene expression dynamics of each experimental condition are well approximated by a linear state-space representation. We then define the dynamics as

$$\begin{aligned} \frac{dx_{\mathrm{on}}}{dt} &= ax_{\mathrm{on}} + bu \\ \frac{dx_{\mathrm{off}}}{dt} &= ax_{\mathrm{off}} \end{aligned} \tag{7}$$

where here x_{on} and x_{off} are scalar variables for ease of analysis. The variables represent the dynamics in the case where the input is present (*on*) and when the input is absent (*off*), respectively. The input u represents the scalar input of a small molecule, e.g. malathion, that drives the expression of genes in the *on* condition through a step input, i.e. $u(t) = 1$ for all $t > 0$. The solution of the linear ordinary differential equations above are given by

$$\begin{aligned} x_{\mathrm{on}}(t) &= e^{at}x_0 + \int_0^t e^{a(t-\tau)} bu(\tau) d\tau \\ x_{\mathrm{off}}(t) &= e^{at}x_0 \end{aligned} \tag{8}$$

where $x(0) = x_0$ for both x_{on} and x_{off}. We want to show that the fold change response is given by the solution of a linear dynamical system. Taking the fold change of x_{on} to x_{off} we have

$$\begin{aligned} x_{\mathrm{fc}}(t) = \frac{x_{\mathrm{on}}}{x_{\mathrm{off}}}(t) &= 1 + \int_0^t e^{-a\tau} \frac{b}{x_0} d\tau \\ &= 1 + \frac{b}{ax_0} - \frac{b}{ax_0} e^{at} \\ &= 1 + \alpha - \alpha e^{at}. \end{aligned} \tag{9}$$

To show that there exists a linear ordinary differential equation (ODE) that gives rise to the above solution $x_{\mathrm{fc}}(t)$, we apply the steps to solve linear ODEs using integrating factors but in reverse order. We know in advance that the integrating factor should take the form e^{at} and we start by dividing both sides of (9) by this integrating factor

$$e^{-at} x_{\mathrm{fc}} = e^{-at}(1 + \alpha) - \alpha. \tag{10}$$

We next differentiate both sides and integrate both sides with respect to t

$$\int \frac{d}{dt}\left(e^{-at} x_{\mathrm{fc}}\right) dt = \int a e^{-at} dt - \int \alpha a e^{-at} dt, \tag{11}$$

then once again differentiating both sides gives

$$\frac{d}{dt}\left(e^{-at} x_{\mathrm{fc}}\right) = a e^{-at} - \alpha a e^{-at}. \tag{12}$$

Applying the product rule to the left hand side, we have

$$\begin{aligned} e^{-at} \frac{dx_{\mathrm{fc}}}{dt} - a e^{-at} x_{\mathrm{fc}} &= a e^{-at} - \alpha a e^{-at} \\ &= e^{-at}(a - \alpha a). \end{aligned} \tag{13}$$

Finally, multiplying through by the integrating factor, e^{at}, and solving for $\frac{dx_{\text{fc}}}{dt}$, we obtain

$$\frac{dx_{\text{fc}}}{dt} = ax_{\text{fc}} + a - \alpha a \tag{14}$$

which is a linear first order ODE, i.e. a linear dynamical system with a step input and $\alpha = \frac{b}{ax_0}$. The importance of this result is to to be able to say that if the dynamics of the transcriptome in each experimental condition are well represented by a linear system, than the fold change dynamics, under the stated assumptions, can also be well represented by a linear system.

We briefly remark on the extension to the multivariate case. Under the assumption that the system dynamics, A, is diagonalizable, the above analysis holds. One such transformation which diagonalizes the the dynamics is given by the set of eigenvectors of A. Formally, if we now have system dynamics with state, $\mathbf{x} \in \mathbb{R}^n$, such that

$$\begin{aligned} \frac{d\mathbf{x}_{\text{on}}}{dt} &= A\mathbf{x}_{\text{on}} + Bu \\ \frac{d\mathbf{x}_{\text{off}}}{dt} &= A\mathbf{x}_{\text{off}}, \end{aligned} \tag{15}$$

applying the transformation $\tilde{\mathbf{x}} = T^{-1}\mathbf{x}$, where $T \in \mathbb{R}^{n\times n}$ is the matrix of eigenvectors of A, results in the transformed systems

$$\begin{aligned} \frac{d\tilde{\mathbf{x}}_{\text{on}}}{dt} &= D\tilde{\mathbf{x}}_{\text{on}} + \tilde{B}u \\ \frac{d\tilde{\mathbf{x}}_{\text{off}}}{dt} &= D\tilde{\mathbf{x}}_{\text{off}}, \end{aligned} \tag{16}$$

where $\tilde{B} = T^{-1}B$. To solve for the fold change dynamics in the multivariate case, we cast the state coordinates into a diagonal matrix, i.e. $\text{diag}(\tilde{\mathbf{x}})$, and compute $\text{diag}(\tilde{\mathbf{x}}_{\text{on}})(\text{diag}(\tilde{\mathbf{x}}_{\text{off}}))^{-1}$. Since the solution in each coordinate is uncoupled from other coordinates, we then have n solutions, each as in Eq. (9).

The case where the above derivation does not hold when the eigenvalues of A have zero real part, i.e. they are exactly zero or have purely sinusoidal response (corresponding to periodic orbits). In this case, the fold change in the coordinate corresponding to zero eigenvalues will approach infinity or it will not be possible to represent the fold change dynamics as a sum of weighted exponentials, e.g. $\tan(x)$. However, such a case would be improbable in a data-driven application for gene regulatory networks. Moreover, any eigenvalue with magnitude zero does not contribute to the dynamics of the system and should be removed from the model.

2 Supplementary Figures

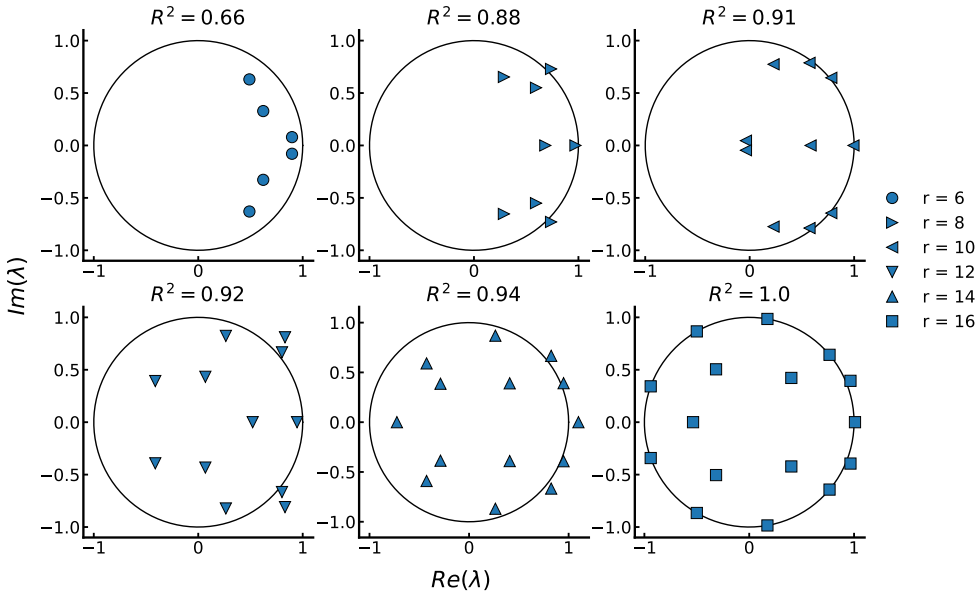

Figure 1: The eigenvalues of the DMD operator plotted in the complex plane for varying number of modes.

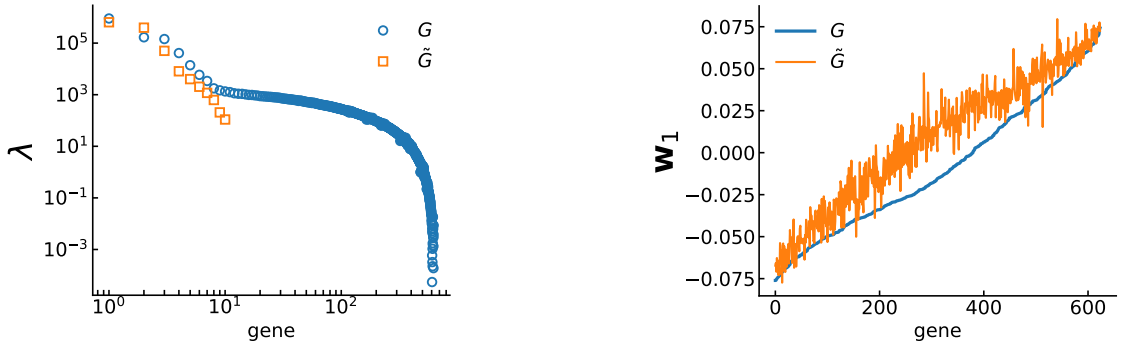

Figure 2: (Left) Approximation of the eigenvalues of the Gram matrix by the reduced order model given by DMD. The full Gram matrix eigenvalues are given in blue circles and the reduced Gram matrix eigenvalues are given in orange squares. (Right) Approximation of the leading eigenvector of the Gram matrix by the reduced order model given by DMD. This eigenvector corresponds to the gene sampling weights in the main text.

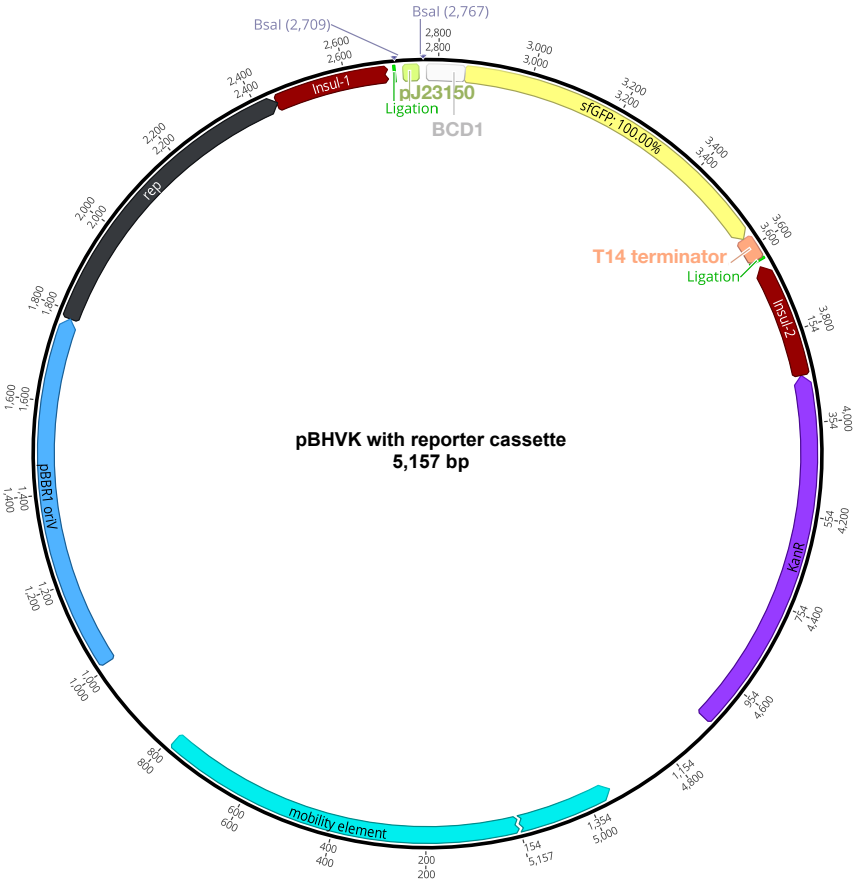

Figure 3: The full plasmid map of pBHVK with the reporter cassette. The two BsaI cut sites on either side of the promoter, pJ23150, are used in Golden Gate Assembly to replace the promoter sequence with a promoter used for malathion sensing. A bicistronic design is used for the ribosome binding site, BCD1. A terminator from the set of Voigt lab terminators is used, T14. For fluorescent reporting, super folder GFP (sfGFP) is used. See Table 3 for sequences of the terminator, ribosome binding site, and sfGFP. See 2 for sequences of the promoters used in the sensor library.

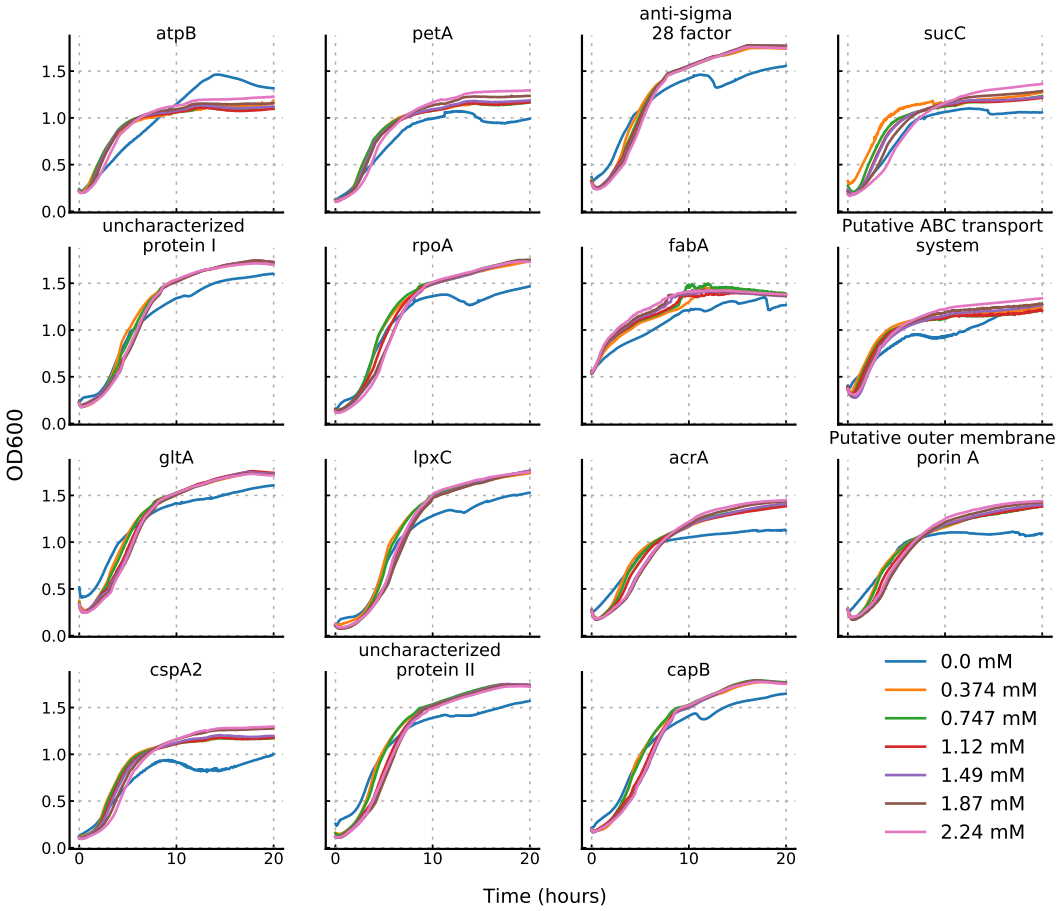

Figure 4: Growth curves of each malathion reporter subject to malathion induction by means of Spectracide.

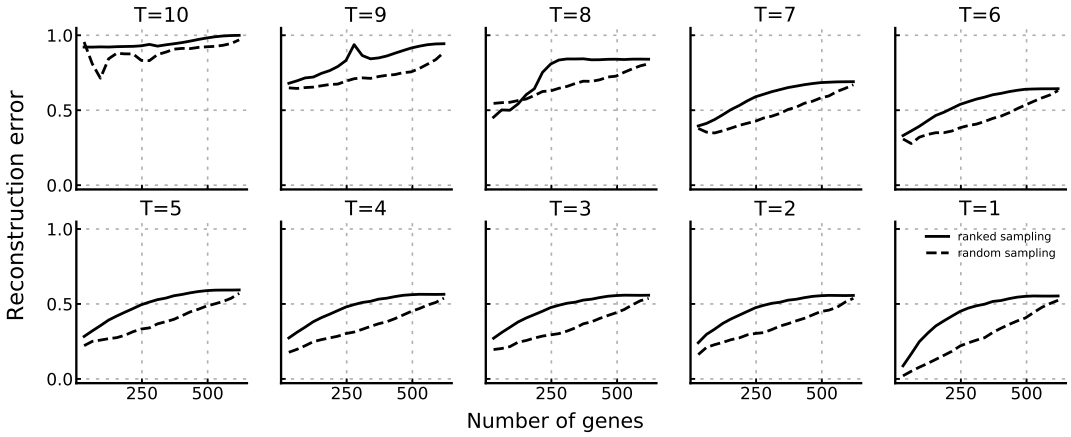

Figure 5: Comparison of the reconstruction accuracy if genes were sampled according to observability ranked sampling (solid line) vs. random sampling (dashed line).

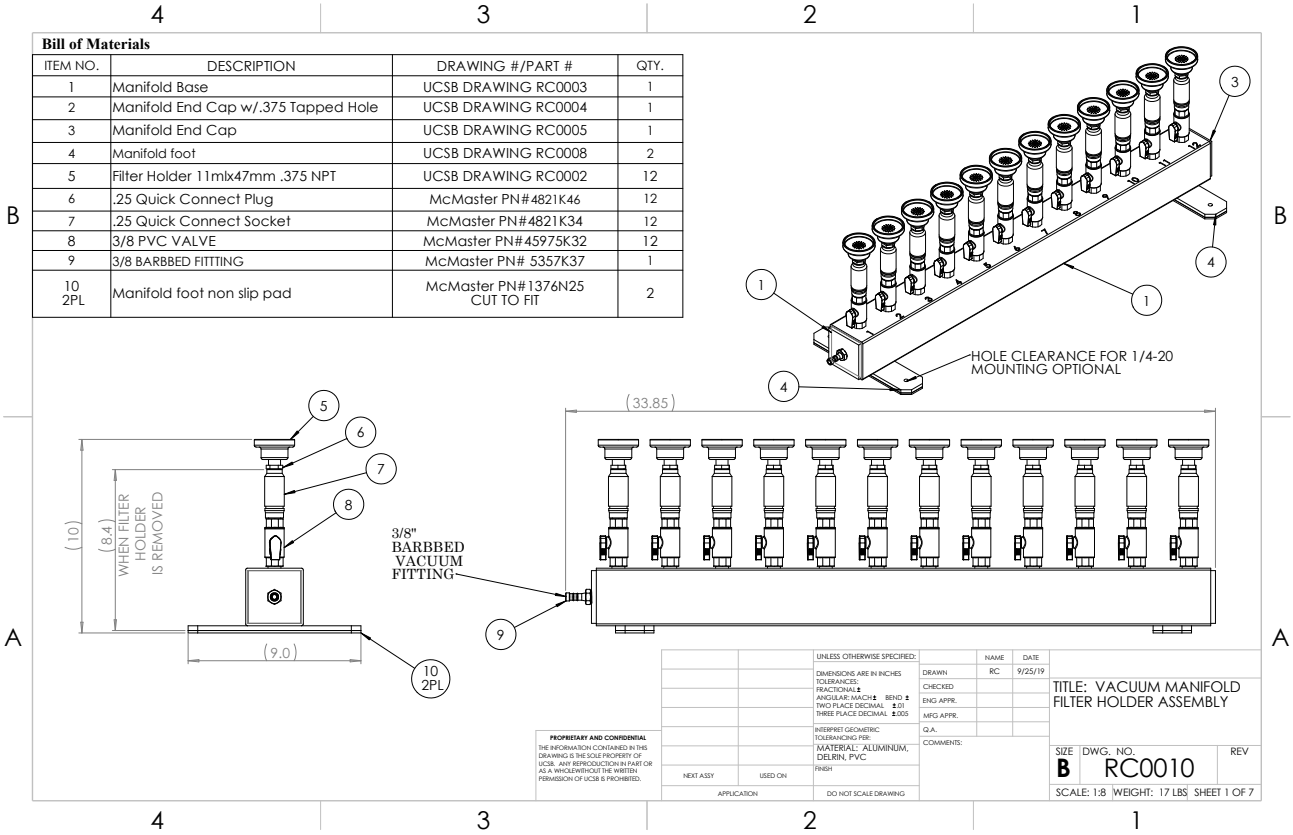

Figure 6: Vacuum manifold design for rapid sampling of mRNA dynamics.

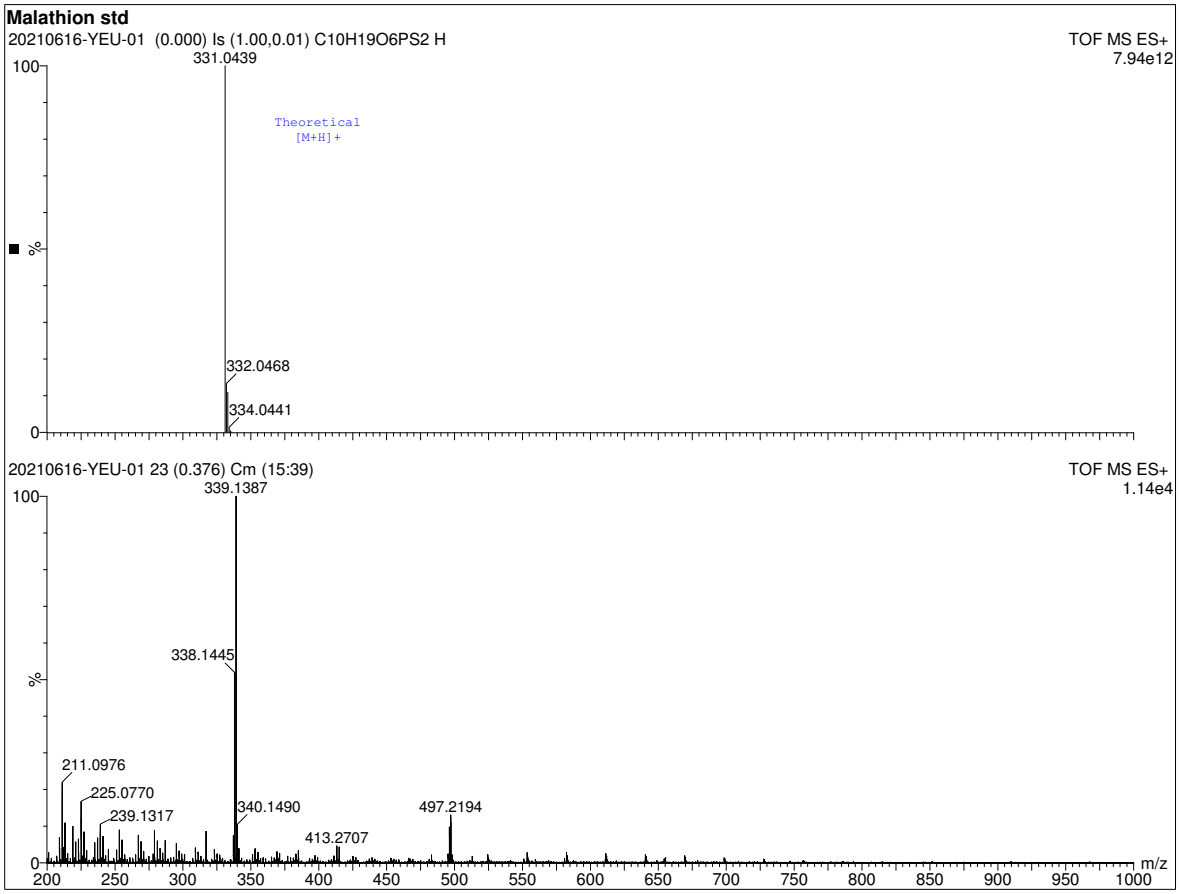

Figure 7: Mass spectrum of malathion (Millipore Sigma Catalog no. 36143) given by time-of-flight mass spectrometry. The theoretical mass spectrum is shown in the upper spectrum and the measured mass spectrum is shown in the lower spectrum.

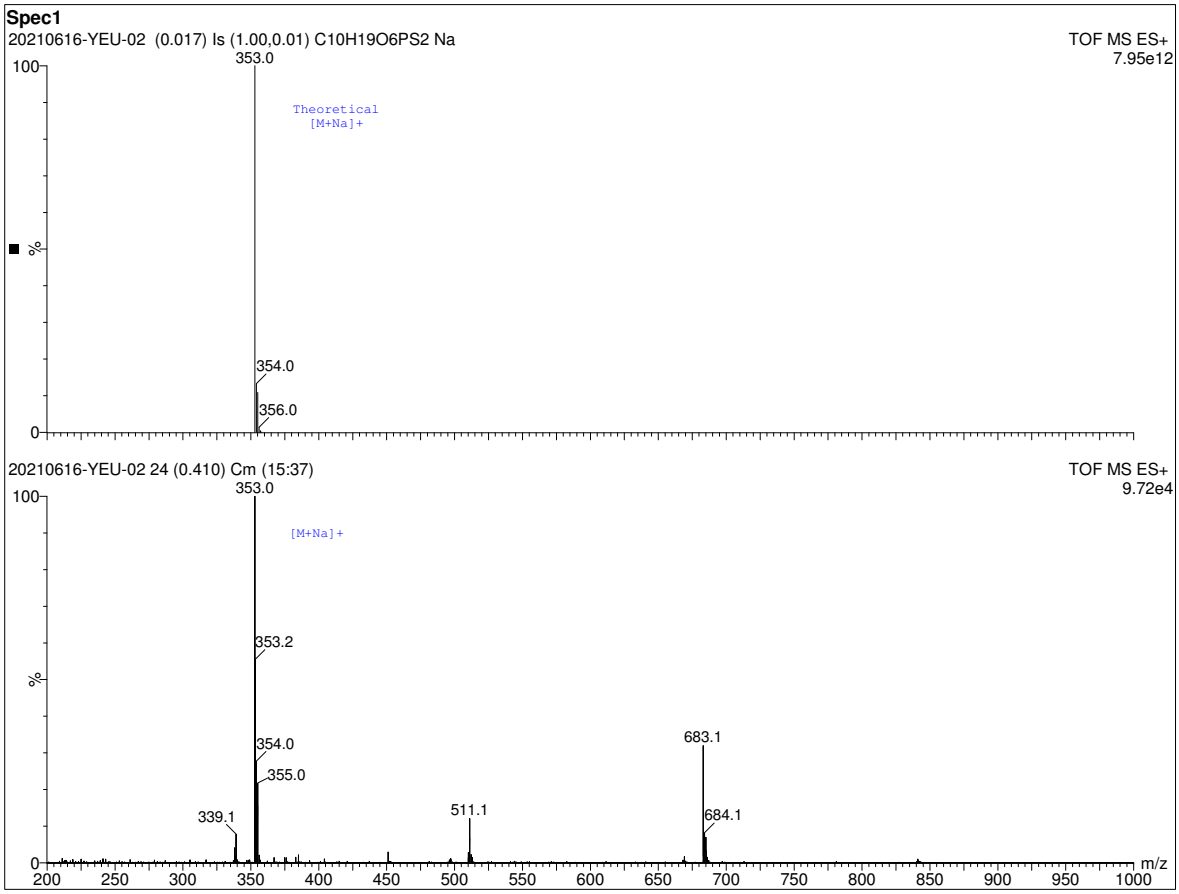

Figure 8: Mass spectrum of Spectracide (replicate 1) (Spectracide Catalog no. 071121309006) given by time-of-flight mass spectrometry. The theoretical mass spectrum of malathion is shown in the upper spectrum and the measured mass spectrum of Spectracide is shown in the lower spectrum.

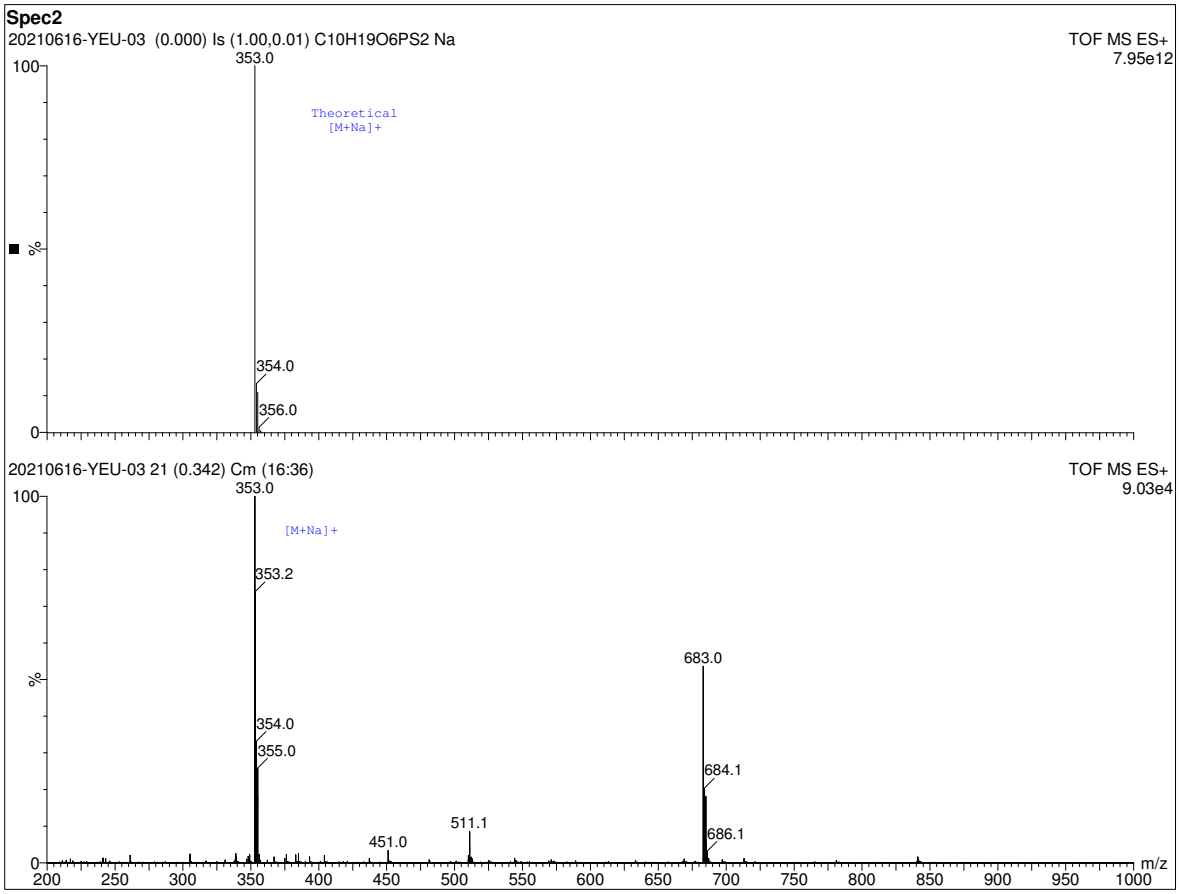

Figure 9: Mass spectrum of Spectracide (replicate 2) (Spectracide Catalog no. 071121309006) given by time-of-flight mass spectrometry. The theoretical mass spectrum of malathion is shown in the upper spectrum and the measured mass spectrum of Spectracide is shown in the lower spectrum.

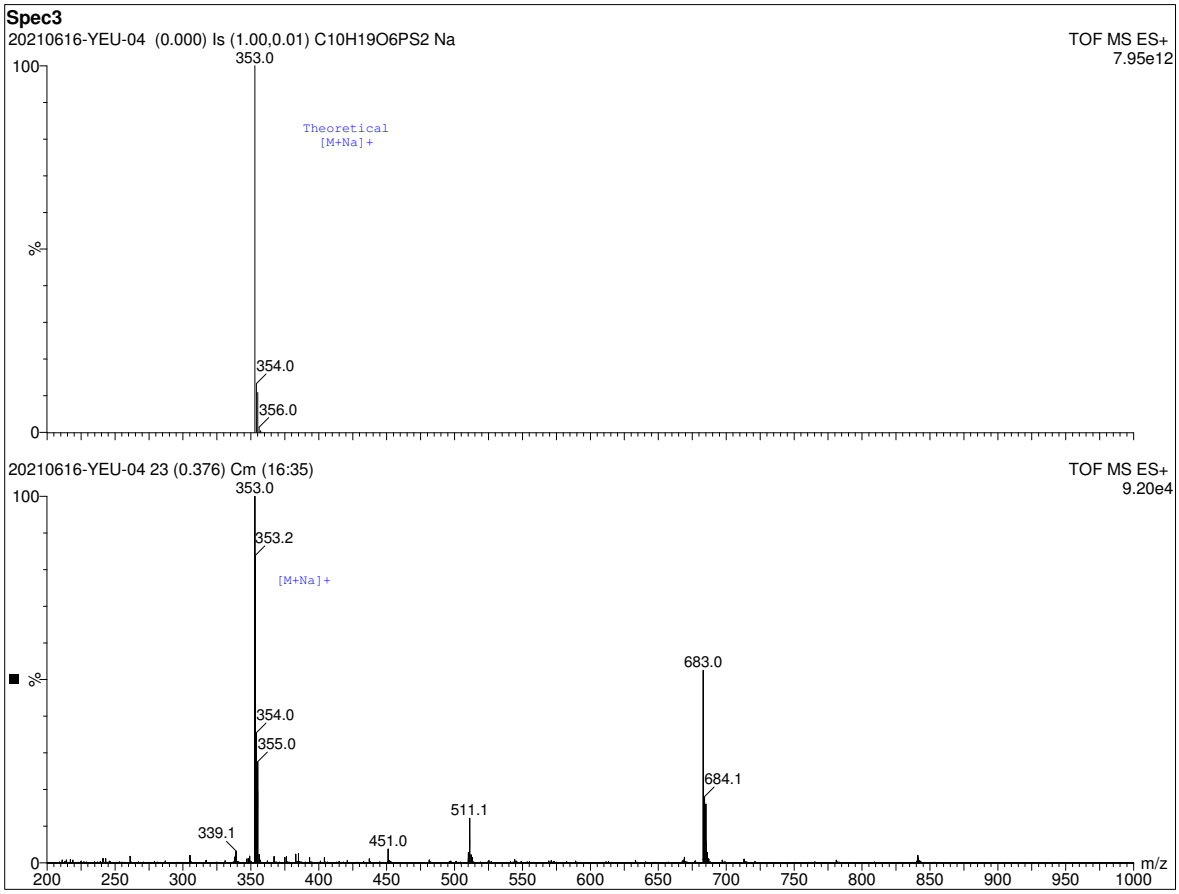

Figure 10: Mass spectrum of Spectracide (replicate 3) (Spectracide Catalog no. 071121309006) given by time-of-flight mass spectrometry. The theoretical mass spectrum of malathion is shown in the upper spectrum and the measured mass spectrum of Spectracide is shown in the lower spectrum.

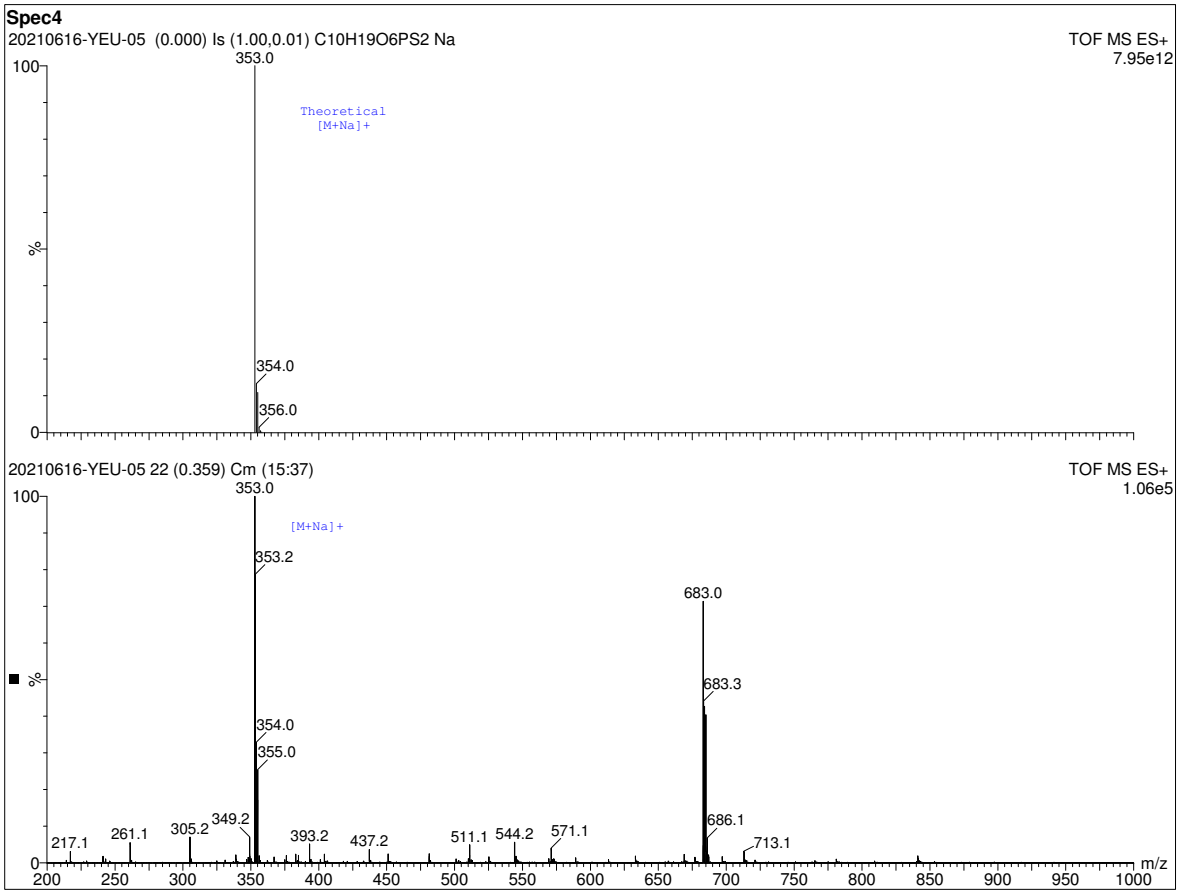

Figure 11: Mass spectrum of Spectracide (replicate 4) (Spectracide Catalog no. 071121309006) given by time-of-flight mass spectrometry. The theoretical mass spectrum of malathion is shown in the upper spectrum and the measured mass spectrum of Spectracide is shown in the lower spectrum.

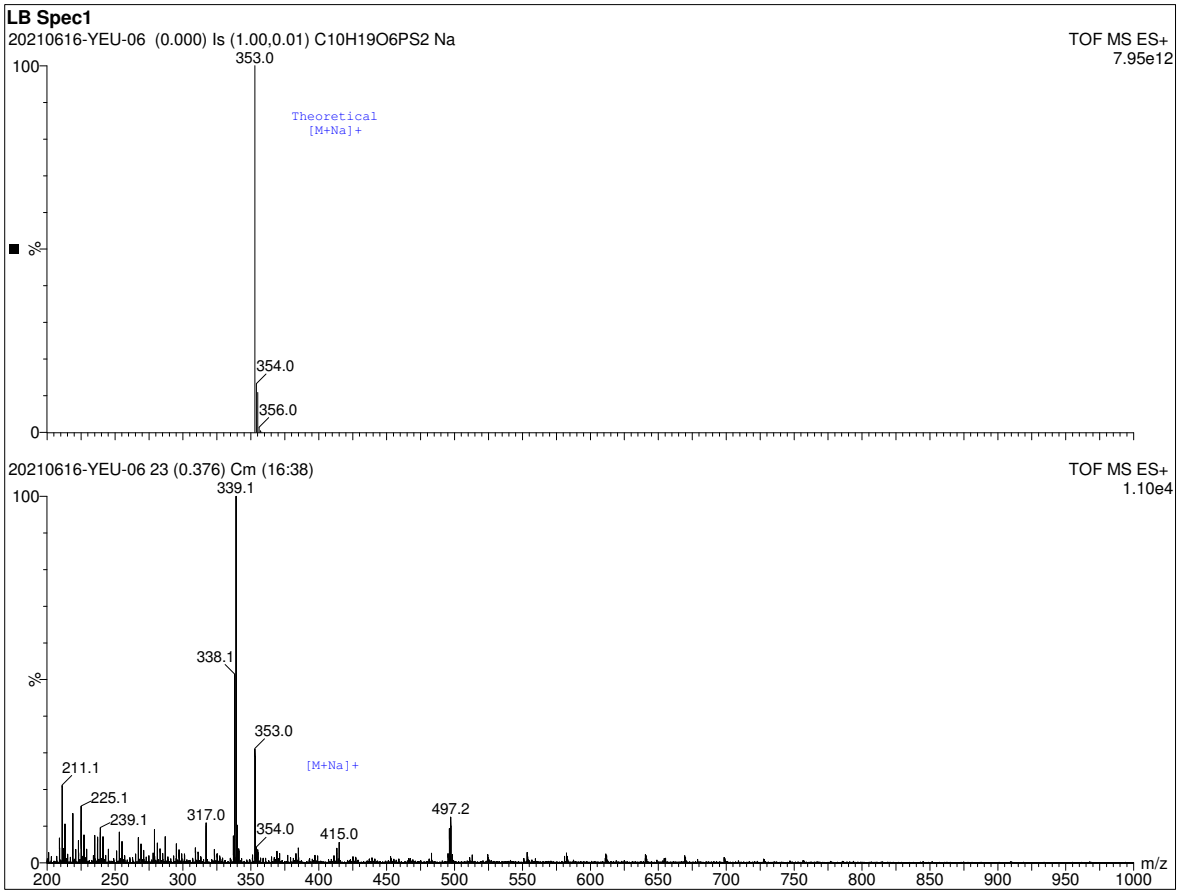

Figure 12: Mass spectrum of a 5% Spectracide in LB broth (replicate 1) given by time-of-flight mass spectrometry. The theoretical mass spectrum of malathion is shown in the upper spectrum and the measured mass spectrum of the solution is shown in the lower spectrum.

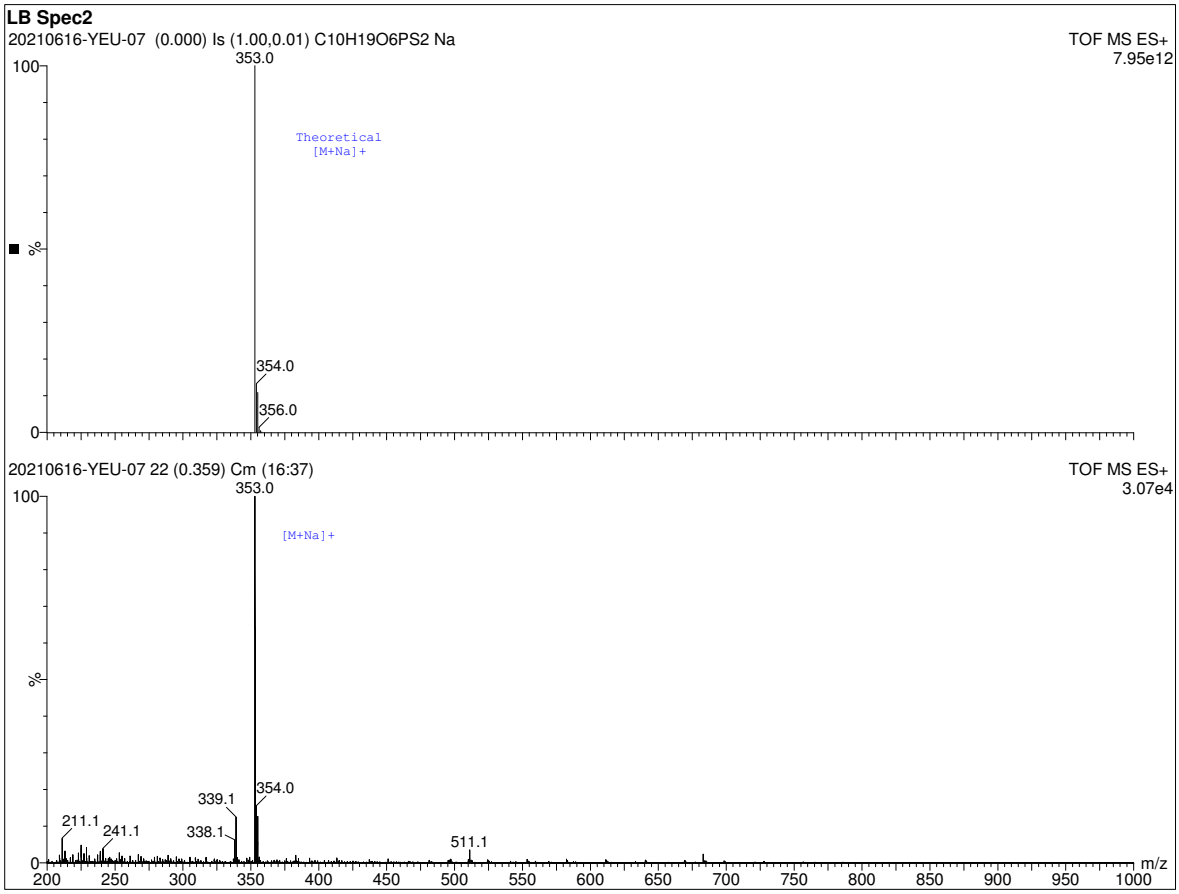

Figure 13: Mass spectrum of a 5% Spectracide in LB broth (replicate 2) given by time-of-flight mass spectrometry. The theoretical mass spectrum of malathion is shown in the upper spectrum and the measured mass spectrum of the solution is shown in the lower spectrum.

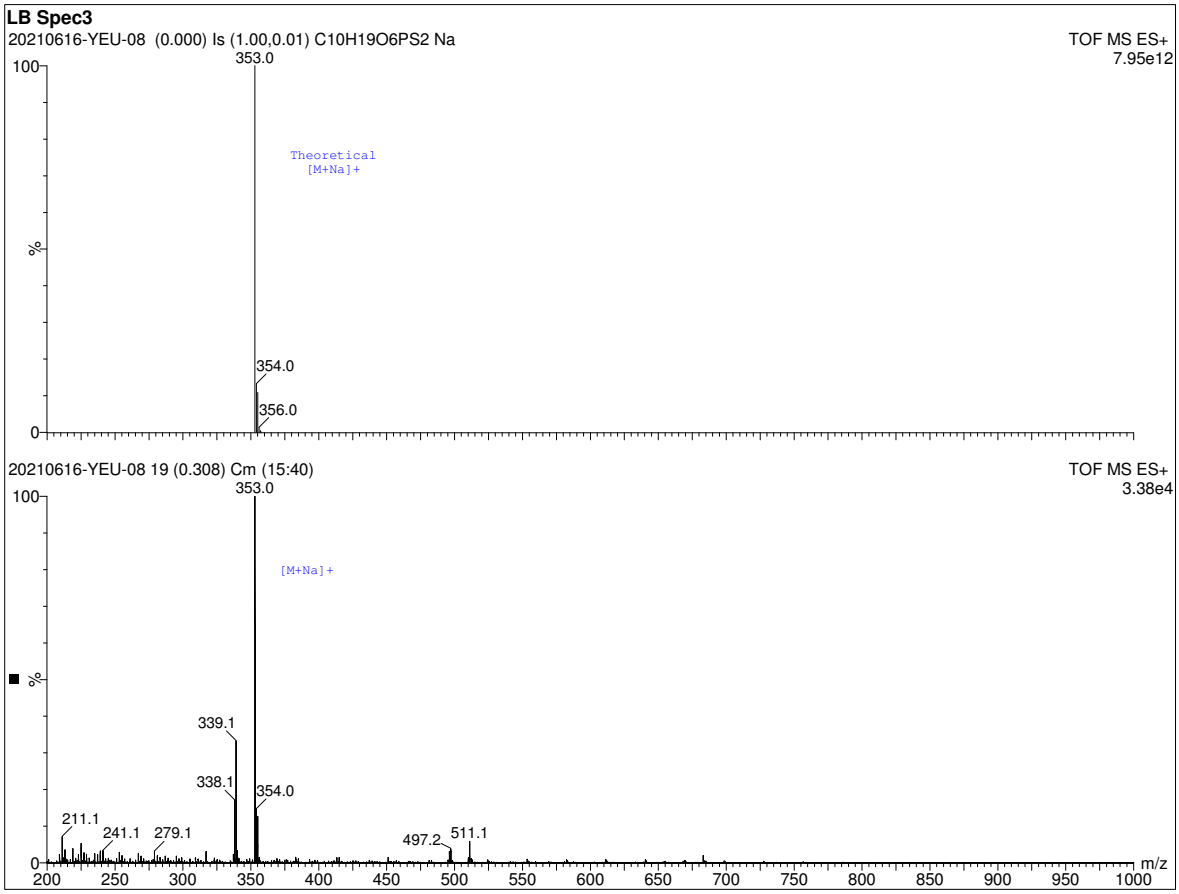

Figure 14: Mass spectrum of a 5% Spectracide in LB broth (replicate 3) given by time-of-flight mass spectrometry. The theoretical mass spectrum of malathion is shown in the upper spectrum and the measured mass spectrum of the solution is shown in the lower spectrum.

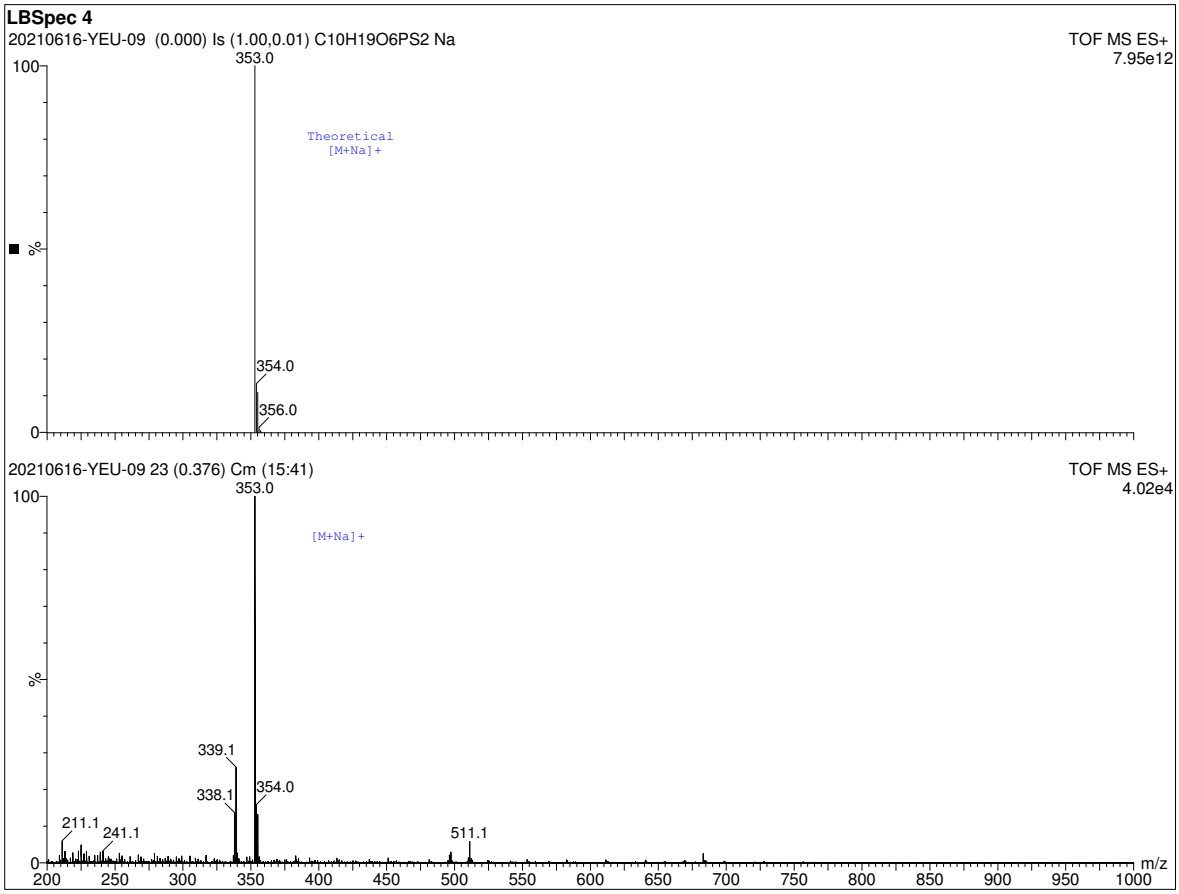

Figure 15: Mass spectrum of a 5% Spectracide in LB broth (replicate 4) given by time-of-flight mass spectrometry. The theoretical mass spectrum of malathion is shown in the upper spectrum and the measured mass spectrum of the solution is shown in the lower spectrum.

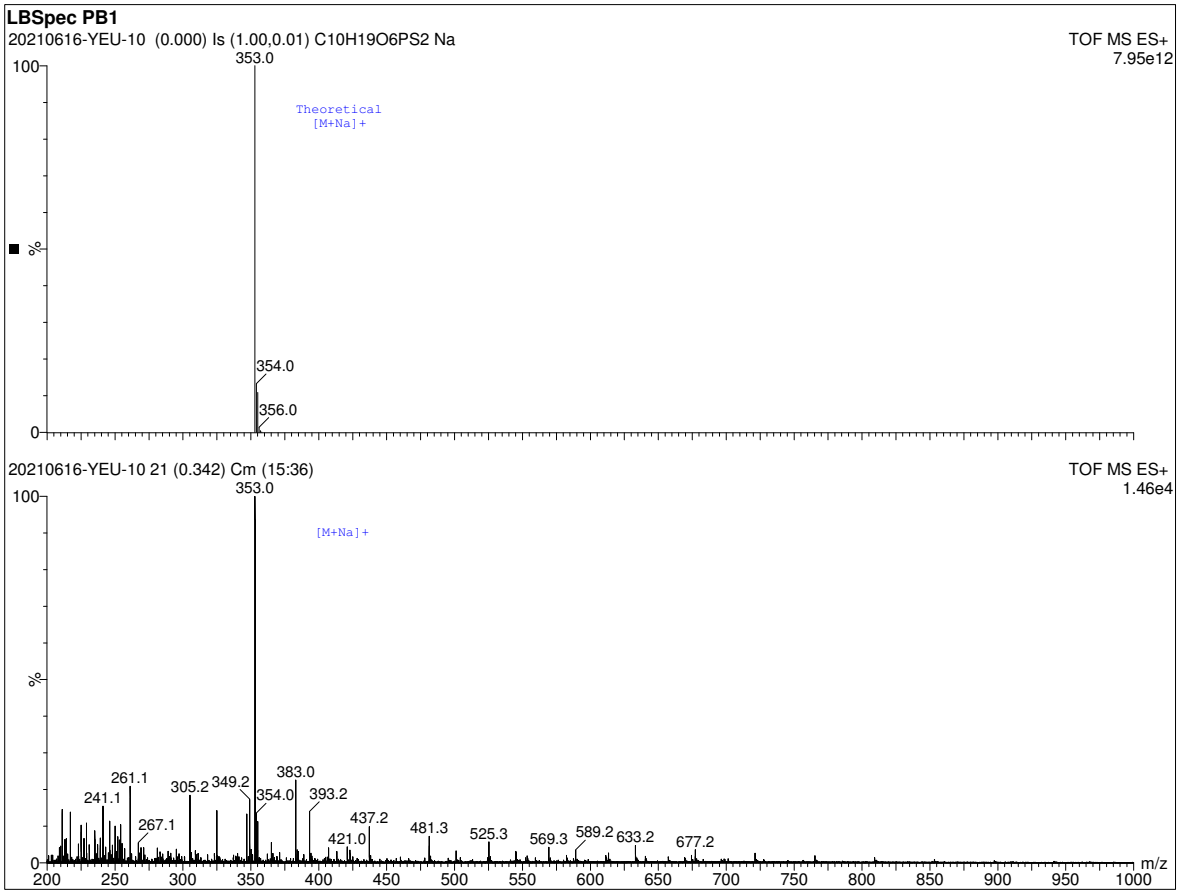

Figure 16: Mass spectrum of a 5% Spectracide in LB broth after photobleaching (replicate 1) given by time-of-flight mass spectrometry. The theoretical mass spectrum of malathion is shown in the upper spectrum and the measured mass spectrum of the photobleached solution is shown in the lower spectrum.

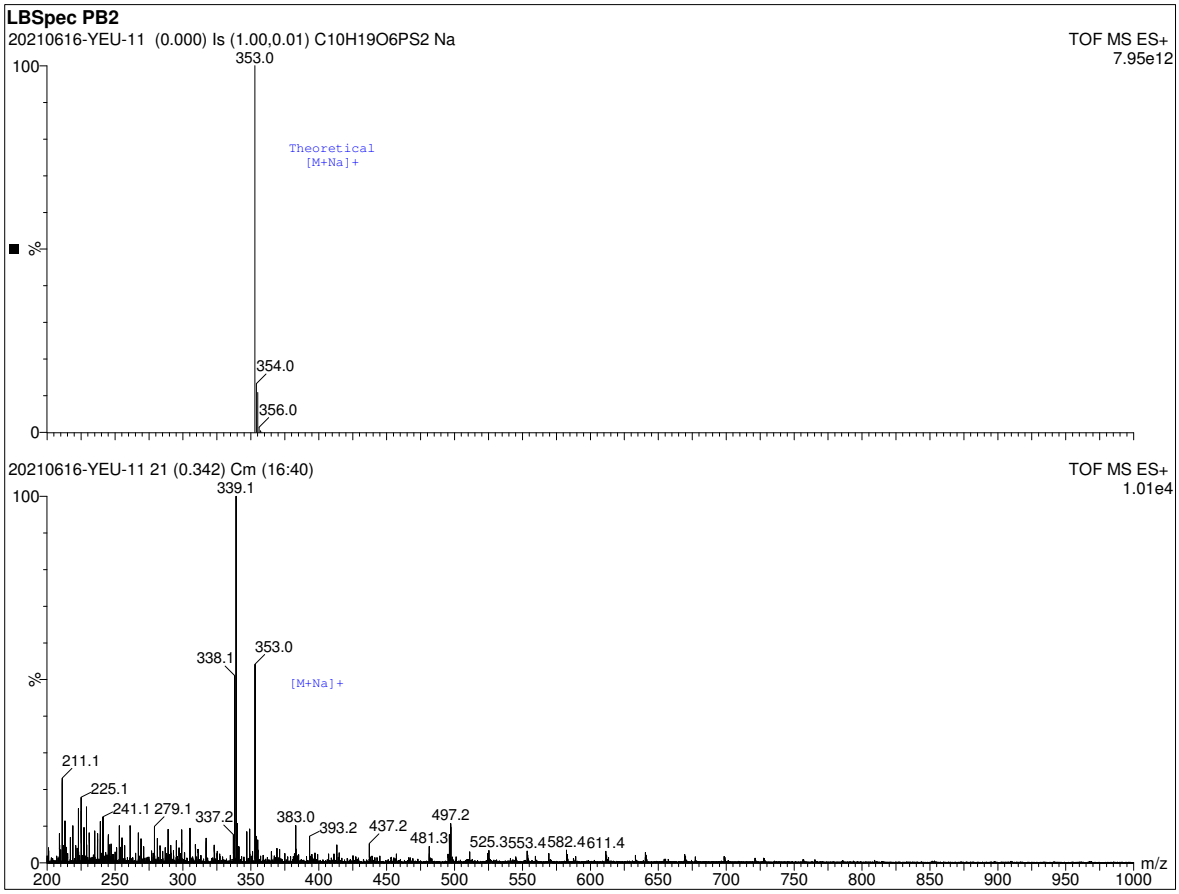

Figure 17: Mass spectrum of a 5% Spectracide in LB broth after photobleaching (replicate 2) given by time-of-flight mass spectrometry. The theoretical mass spectrum of malathion is shown in the upper spectrum and the measured mass spectrum of the photobleached solution is shown in the lower spectrum.

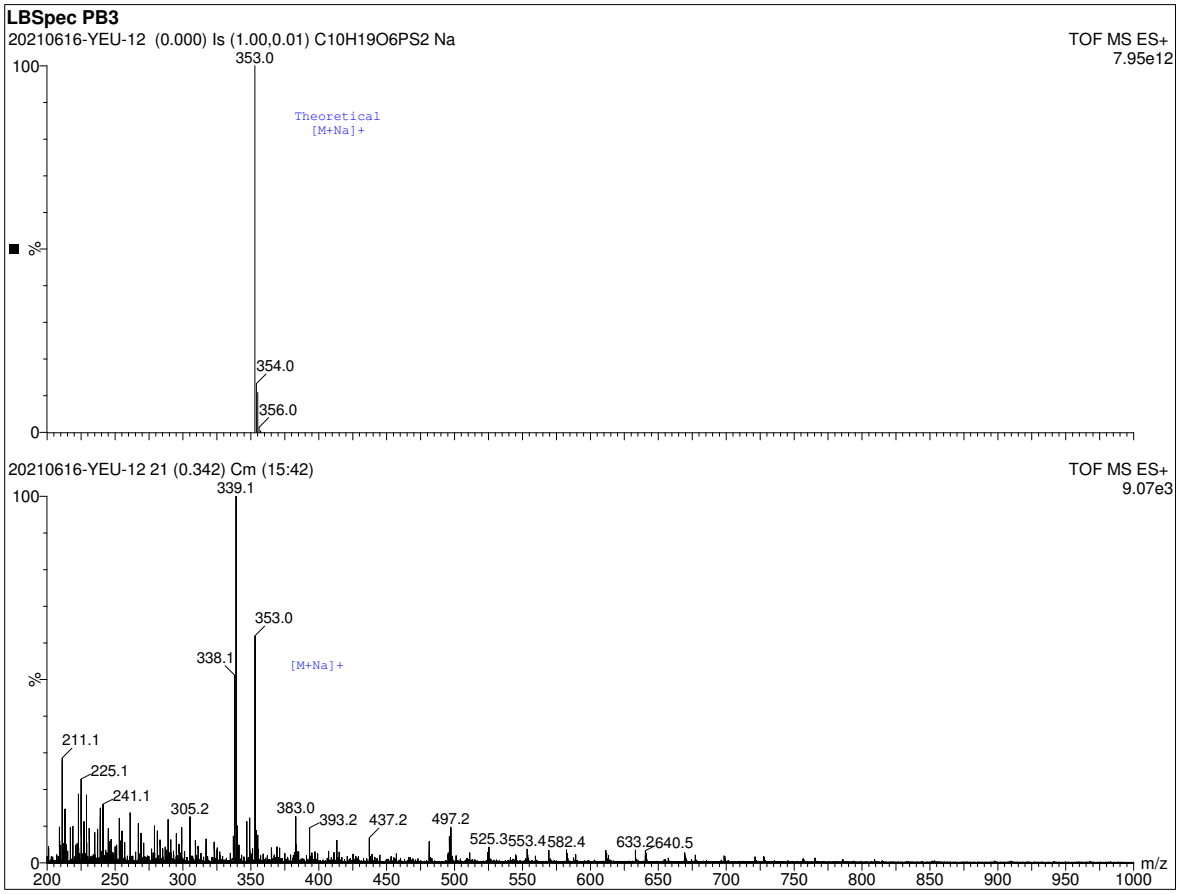

Figure 18: Mass spectrum of a 5% Spectracide in LB broth after photobleaching (replicate 3) given by time-of-flight mass spectrometry. The theoretical mass spectrum of malathion is shown in the upper spectrum and the measured mass spectrum of the photobleached solution is shown in the lower spectrum.

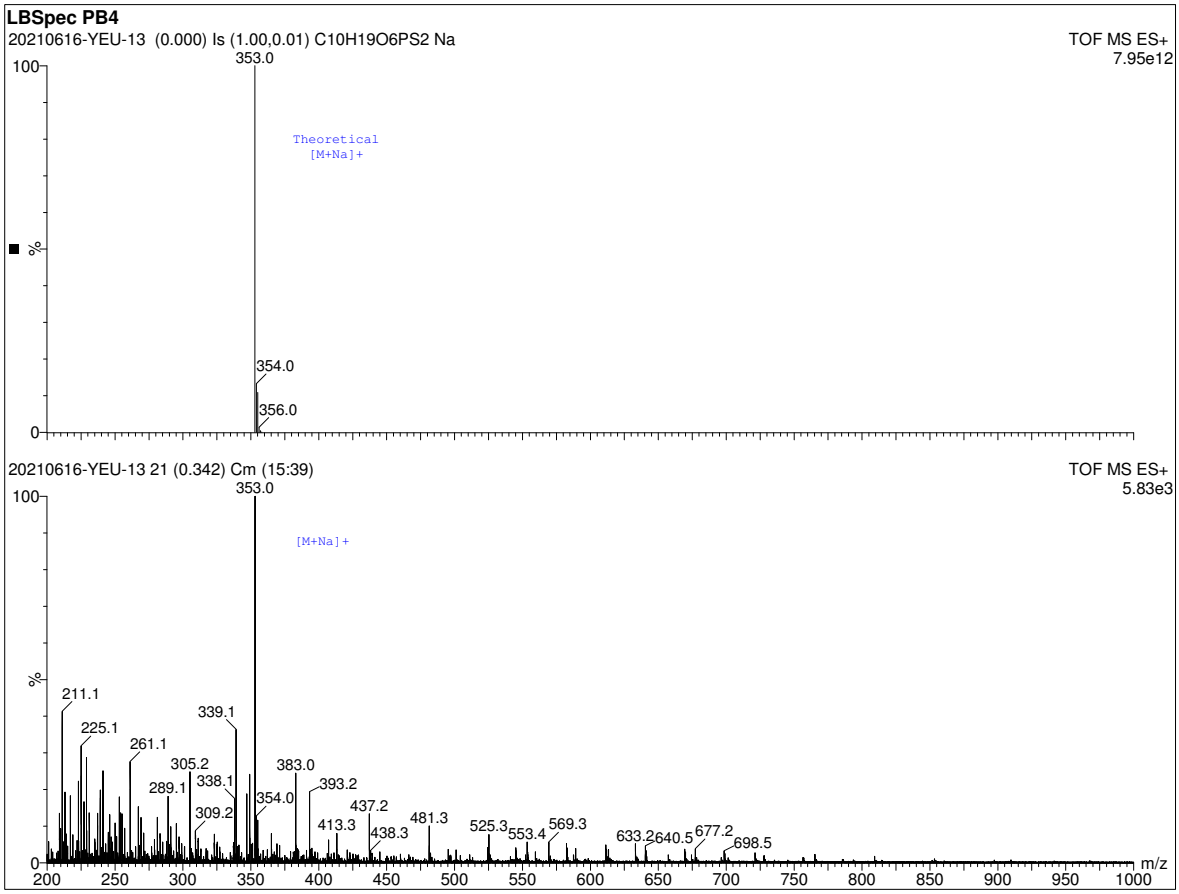

Figure 19: Mass spectrum of a 5% Spectracide in LB broth after photobleaching (replicate 4) given by time-of-flight mass spectrometry. The theoretical mass spectrum of malathion is shown in the upper spectrum and the measured mass spectrum of the photobleached solution is shown in the lower spectrum.

3 Supplementary Tables

Time point (minutes)	OD_{600}	Volume harvested (mL)	Malathion induction
0	0.5	10	
10	–	10	**X**
20	–	10	
30	–	10	
40	–	10	
50	–	10	
60	1.0	10	
70	–	10	
80	–	10	
90	–	10	

Table 1: Metadata for the time-series RNAseq experiment.

Sensor	Strand	Loci	Promoter sequence
PFLU_6124	Antisense	6709164 - 6709017	AACATTTGCTTATGTAGCGCGTGATCGGAAATCACTAC CCGGCAGTTGAATAGGGGCAGAACCGCCCCTATACTCT GCGCGCATTTTGTCGGCACAAATTATGCCAAGTTATTG ATTTCCGGCAGCCGACCATTGAGGAGCAAGAGTG
PFLU_0841	Sense	950865 - 951131	TTCGCTTTACGTTCCACAAAAACGCCCAGCCTCCTCAC GGAGCTGGGCGTTTTTTATTGCCTGCGATTTATACACA AATTTCGCCGTGACAACTTGCCACATCCGTAGACCCCC TATACTACAAGGCCTGGAGGCTGAGCCCAGGGCAATTC CCTTGTCATACGTGGGGCTTTTCATTACCATTCGGCAA AATTTTTATAAGTAAAGATTCAACACTTAGTAGACGCC TGATTTAACAGGCCAAAAAAGCTGATGGGAGAGGACT GA
PFLU_4736	Sense	5213048 - 5213188	AGTGCTGGCAGAGGACGCTGGGTTTTTCTACACTGTGC ACGAGATATTCCGTGCGCAGATTTATTGTCATTCGCGC CTAAAGTTCGTCCGGGTATTGCCGAAAACATGGCAAGC GTCCAAATACCCAGAGGTTTTTTGATC
PFLU_1823	Sense	1989934 - 1990137	GCGAGATAATAAGAAACCACGGCGGAGTTGCCCGTCG TGAGCCTTGCGCGCAAGACTCACCGCGGAATATCCGCT GGACGCAGTCTTGCGCAGCTTTACGGGCCTTGAGCCCC GCAAGCTGCGCAAGCAGCAGTCACAGGTGGCGCGGCA CTCATAATGAGCGCAGCGCCGAATGCGCAGTACCTAAC GAAGACGGTAAAAAGC
PFLU_3761	Antisense	4158693 - 4158135	CTGTGACACGTCGCCAAGGCAGGCGCGGCGGATAGTT TCAGTTCGGCGTCATACAAGTGCACTGCACCCCACTTC ATCGTGGCCGTTTGCGAAAGCGATTGTCCGCTTGCGAC GCGGCACAATCAGGGTATGTGCGCAGCTTGGCTTCCCA GTAATTGCCCCATTAAATTTGTGGCTTTTCTGACGAGC TTTTACTCGTCATCTCTTTGTTTTTTTACTATTATCGT TCACCTGCGCACTCAAGGAAGAGAGGCTGAGCGCCTTG AGGCTGGTAGAAAATTCATACTCGATCACTGAACGAGT TATTGCTTTTACCCAGAACCTAACGACTCAGCCAACCA TAAATACCTCTTGGTGAAACCGATGGATAAAATGTGTG GCATCGTTGTAGTGGTAGGAC
PFLU_5502	Antisense	6038217-6038089	GTGTGATCCGCTTGAAGCCCGGCAGCTAGTGCGCTGCC GGGTTGATTATTTGTTATTACAGCGATATTATCTCGCG CCCTATTTCTTGGCTTCCGGGGCGTAGGTAGCTGTCAA TTGGAGTCCCACTGA

PFLU_1836	Antisense	2003829 - 2003581	CGCCGCGCCATCAGCCAACTCCGACTGGCGTGAAAGAC GAAAGTGCGGCAGTCTTAGGCACCCGAACGGGCCCAT AAACAGGCCCGGTTTAAAATTTCAGTGAACAAGTGTA CATTCAGTACCTTGCCGCTGTGACTTTCACTACAACGC AATAGTCTATGTGTAGGCTGCCGACATGAGGCATGAAC GCTTCATTCGGTTCGGGAAGATTTGCCCTACCCTGCCG CATGGGATTATTGAGGAGCTCGC
PFLU_0376	Sense	417961 - 418174	AAGTCATAACTGCTTACACATCAACCGGTTGCCGGTAC TCCTCTGCGTAAGTGTCTGCCCCTGAGCTTTGCCGCAC CGATGTGGGGCTTTTCCGACATATGCCGATAACAAATA GCCGTGAAACCTTTGTGACGAGCAACGAGTGGGTTAG GATCGCACCCCGAAATGGTGCAGCCCTTTTGCGCGCCG ACCTTACAAAAATCGTTCAGGGGAC
PFLU_1815	Antisense	1980804 - 1980440	GGCTTTTTTTCACACTGAAGAGCCCCTAACAATCAGGG CAAAGTTGTTGGGGAGTGCGACTGGTCAGGTAAGCAC CACCCAGGGAGTGCGACCCCCAATGAAAGCAAGCCCA AAAGCCCTTGGCGGTCGGTGGCCGAGTATAGACAGTT AGGTTACTAATGACAACGCGCACTCCTCACCCTAATAG CTGATTGCGCTGGCGGGATAAAAGGCGTAAATGGCGC TCAATTTCGAGGAAAAAGTACGGTTAAAGCCTTCTGGG GCAAGACTTTAGGCAAATTGACATCTGAATTTATCTCA CTATAGTGGTGCGGGCCCTGCGTGGGGGGTCTGTCTG ATGATTTGAAGCATAAATAGGAGGCCAC
PFLU_0953	Sense	1058342 - 1058453	TGGAATGTATCAGGGCTATGAAGGTGATTGGTGTTCA GCAAAGGTCTGGTCTGCTATTATCGCCAGCCTTTGTTG ATACCAGTTCGCAATTTGCGCTGAAGCGGTCCAAGCC
PFLU_1380	Antisense	1527252 - 1526967	GGCAGTAAAACCTCAATCAGGACACTGGGGGCTATCG TTAACGCAACGTTAATAGACGTAAACGATCATCCGAAT ATTTGTGGGACGACACCGTCATGGGTGCCGAACGTAAT GGAATCGAGGCTTCGGGCGTTGCTTTGTCAACACTCCG CGAAGCCTGTCAAGAGTTTACAAACAACCATGAACGTA AGTATATTGCGTAGCAAGCTACTTATCCACTCACAGCT TGTTTTTTACCCTTCCACACTTCTTGTGCGCACCCTGC GCGCCTGACCCGAGGATCTTC
PFLU_4612	Antisense	5088655 - 5088549	TGCGTGGCAAATATCTCTTACGTGTAGGCAAGTTCTGT TAGACTTGTCGCCGAGTTGTCCCCCGGTTTGTGGGACT GCTTTACAATCACCAGATGGGGATTTAACGG
PFLU_4150	Sense	4592631 - 4592843	GATTTGCCGCTGATCTCACGGCTTTTTTGGCGGTAAAA CAGGCTTAAAACTGCCGCTTCTCACAAATTACGCAGCT TTTACGGCTTTTTTTACCAGTTGATATTTCGAGCCAAA GCCCCGTAAATCGGGGCTTTCAGCCGGATCAGGCACTA AACGCAACGCTATTGATTAGCAAACAATGCCTTGGGGG GGCTCCCAAGCCGAACATTTCGACTATGATAGCCCGGT GTGCCCAGTTGGCCTGAGCAGCACAGCACTACTGAAAA TATATGTTTCTTGGAGATACACC
PFLU_1302A	Antisense	1440968 - 1440759	GGCGGGTGTCCTGAATAGCGAGGTGGAAAAATACTGT GGGGCATCTTACCGGGGCCGGCGTTGGGGTTCAAAGG TCACAGGGCTTTTCTTGATGAATGCGCCGGCGGCTATA AGCCGCAGCCAGCGGGGCCGGGGTTAATATTGCCGCG CAGGGCGACCGTGGATACCACCGTCAGTCACGAATTTA GAGAAACCTTCGGAAATACCATTGGCACGTTCCGGAAA AAGGGTTAAGGTGGCGCCACTGTGCTGCTTGTGTCACT GAGAATCTCTACACGATATGTTGAATTTCGATCCAACC ATCTCCAAGAATTTTTCCTGCTCTTTGCACTCAGTCTC GGCCAGGGCTTTTCCTGAGTCGCAGTTAACTTTGTCCA AGGAGATACACC

PFLU_1358	Sense	1498195 - 1498311	AACAGCCTGCATCCATTGATGCAGGTCAGTTATTGCCC TTCTTTACGCTCCGTCGTGGGCGACATTGATCCCCGTC AATTTTCCAATCCGCCTTCTGCATTAACTTAGCCCTAT CGCAACAGGGCAAGTGCAGGAGGCCGGTC

Part	Sequence
BCD1	GGGCCCAAGTTCACTTAAAAAGGAGATCAACAATGAAAGCAATTTTCGTACTGAAACATCT TAATCATGCACAGGAGACTTTCT
T14	AACGCATGAGAAAGCCCCCGGAAGATCACCTTCCGGGGGCTTTTTTATTGCGC
sfGFP	ATGCGTAAAGGCGAAGAGCTGTTCACTGGTGTCGTCCCTATTCTGGTGGAACTGGATGGT GATGTCAACGGTCATAAGTTTTCCGTGCGTGGCGAGGGTGAAGGTGACGCAACTAATGGT AAACTGACGCTGAAGTTCATCTGTACTACTGGTAAACTGCCGGTACCTTGGCCGACTCTGG TAACGACGCTGACTTATGGTGTTCAGTGCTTTGCTCGTTATCCGGACCATATGAAGCAGCA TGACTTCTTCAAGTCCGCCATGCCGGAAGGCTATGTGCAGGAACGCACGATTTCCTTTAAG GATGACGGCACGTACAAAACGCGTGCGGAAGTGAAATTTGAAGGCGATACCCTGGTAAAC CGCATTGAGCTGAAAGGCATTGACTTTAAAGAAGACGGCAATATCCTGGGCCATAAGCTG GAATACAATTTTAACAGCCACAATGTTTACATCACCGCCGATAAACAAAAAAATGGCATTA AAGCGAATTTTAAAATTCGCCACAACGTGGAGGATGGCAGCGTGCAGCTGGCTGATCACT ACCAGCAAAACACTCCAATCGGTGATGGTCCTGTTCTGCTGCCAGACAATCACTATCTGAG CACGCAAAGCGTTCTGTCTAAAGATCCGAACGAGAAACGCGATCATATGGTTCTGCTGGA GTTCGTAACCGCAGCGGGCATCACGCATGGTATGGATGAACTGTACAAATGATGA
5' overhang	GAACGGTCTCAGCAT
3' overhang	GTCGTGAGACCTTACG

Table 3: Sequences for the parts used in the reporter cassette.

Malathion reporter	Locus tag	Time point (hours)
atpB	PFLU_6124	1.0
petA	PFLU_0841	2.0
anti-sigma 28 factor	PFLU_4736	3.2
sucC	PFLU_1823	8.1
Uncharacterized protein I	PFLU_3761	12.9
rpoA	PFLU_5502	15.0
fabA	PFLU_1836	14.0
Putative ABC transport protein	PFLU_0376	0.9
gltA	PFLU_1815	3.2
lpxC	PFLU_0953	0.7
acrA	PFLU_1380	3.1
Putative outer membrane porin A protein	PFLU_4612	2.0
cspA2	PFLU_4150	2.4
capB	PFLU_1302A	8.5
Uncharacterized protein II	PFLU_1358	5.6

Table 4: The time points at which the Hill functions are fit to each reporters' response.